

Robust Decadal Variations in ENSO Diversity, and its Impact on Future Scenarios

Bastien Dieppo (✉ bastien.dieppo@gmail.com)

CAWR - Coventry University <https://orcid.org/0000-0001-7052-1483>

Antonietta Capotondi

NOAA Earth System Research Laboratory

Benjamin Pohl

Biogéosciences <https://orcid.org/0000-0002-9339-797X>

Kwok Chun

Department of Geography, Hong Kong Baptist University

Paul-Arthur Monerie

University of Reading <https://orcid.org/0000-0002-5304-9559>

Jonathan Eden

CAWR - Coventry University

Article

Keywords: El Niño-Southern Oscillation (ENSO), diversity

Posted Date: April 15th, 2021

DOI: <https://doi.org/10.21203/rs.3.rs-387048/v1>

License:  This work is licensed under a Creative Commons Attribution 4.0 International License.

[Read Full License](#)

Version of Record: A version of this preprint was published at Communications Earth & Environment on October 7th, 2021. See the published version at <https://doi.org/10.1038/s43247-021-00285-6>.

1 **Robust Decadal Variations in ENSO Diversity, and its Impact on Future**
2 **Scenarios**

3 Bastien Dieppois^{1,2*}, Antonietta Capotondi^{3,4}, Benjamin Pohl⁵, Kwok Pan Chun⁶, Paul-
4 Arthur Monerie⁷, Jonathan Eden¹

5

6 ¹ Centre for Agroecology, Water and Resilience, Coventry University, Coventry, UK

7 ² Department of Oceanography, MARE Institute, University of Cape Town, Cape Town,
8 RSA

9 ³ Cooperative Institute for Research in Environmental Sciences, University of Colorado,
10 Boulder, Colorado, USA

11 ⁴ Physical Sciences Laboratory, NOAA, Boulder, Colorado, USA

12 ⁵ Centre de Recherches de Climatologie, UMR 6282 Biogéosciences, CNRS/Université de
13 Bourgogne Franche Comté, Dijon, France

14 ⁶ Department of Geography, Hong Kong Baptist University, Hong Kong, China

15 ⁷ Department of Meteorology, National Centre for Atmospheric Science (NCAS), University
16 of Reading, Reading, UK

17

18

19

20

21 *Correspondence to: Bastien Dieppois, Centre for Agroecology, Water and Resilience

22 (CAWR), Coventry University, Ryton Gardens, Ryton on Dunsmore, Coventry, CV8 3LG,

23 UK. E-mail: bastien.dieppois@coventry.ac.uk

24

25

26 **Abstract**

27 El Niño-Southern Oscillation (ENSO) shows a large diversity of events, whose modulation by
28 climate variability and change, and their representation in climate models, limit our ability to
29 predict their impact on ecosystems and human livelihood. Here, we introduce a new framework
30 to analyze probabilistic changes in event-location and -intensity, which overcomes existing
31 limitations in studying ENSO diversity. We find robust decadal variations in event intensities
32 and locations in century-long observational datasets, which are associated with perturbations
33 in equatorial wind-stress and thermocline depth, as well as extra-tropical anomalies in the
34 North and South Pacific. A large fraction of CMIP5 and CMIP6 models appear capable of
35 simulating such decadal variability in ENSO diversity, and the associated large-scale patterns.
36 Projections of ENSO diversity in future climate change scenarios strongly depend on the
37 magnitude of decadal variations, and the ability of climate models to reproduce them
38 realistically over the 21st century.

39

40 **Introduction**

41 El Niño-Southern Oscillation (ENSO) is the leading mode of tropical climate variability, with
42 impacts on ecosystems, agriculture, freshwater supplies and hydropower production spanning
43 much of the globe¹⁻³. The majority of impact studies, including seasonal to multi-year
44 predictions, have developed from a “canonical” representation of ENSO, as characterised by
45 sea-surface temperature anomalies (SSTa) in the central-eastern Pacific⁴⁻⁶. However, ENSO
46 shows large differences from one event to another in terms of its intensity, spatial patterns and
47 temporal evolutions⁷⁻⁹. For instance, while the 1997/98 El Niño displayed extreme SSTa in the
48 eastern equatorial Pacific (EP-ENSO), the largest SSTa in the winter of 2002/03 were weaker
49 and primarily confined to the central equatorial Pacific (CP-ENSO). Differences in the
50 longitudinal location and intensity of ENSO events are sensitively associated with different

51 impacts on regional climate throughout the world^{10,11}. Such differences in ENSO patterns,
52 referred to as “ENSO diversity”⁷, and their representation in climate models thus strongly
53 influence the skill of impact prediction systems¹², and underscore the need for an appropriate
54 characterization and further mechanistic understanding of ENSO diversity.

55

56 The post-1990s increases in the frequency of CP El-Niño events¹³⁻¹⁵ has led some researchers
57 to associate such changes in ENSO patterns to the influence of global warming¹⁶. However,
58 the role of natural low-frequency climate variations may also be important for altering ENSO
59 characteristics¹⁷⁻¹⁹. Indeed, observations and climate models show the presence of decadal
60 modulations in both intensity^{17,19,20} and pattern diversity²¹. In particular, different phases of the
61 Pacific Decadal Oscillation (PDO)^{18,22} and the Atlantic Multidecadal Oscillation (AMO)²³ were
62 considered more conducive to either CP- or EP-ENSO. However, to date, no robust decadal
63 variation in event locations has been detected in long-term observational records^{24,25}. Similarly,
64 we know very little about the ability of climate models to realistically reproduce ENSO
65 diversity and its low-frequency variability^{7,8}. CMIP3 and CMIP5 models showed large biases
66 in the background mean state of equatorial Pacific SST, leading to an excessive westward
67 extension of the ENSO patterns²⁶⁻²⁸, and limiting the models’ ability to simulate realistic ranges
68 of ENSO diversity^{9,29}. Further research is thus needed to determine how these decadal
69 variations may affect the reported historical and future strengthening of ENSO³⁰⁻³², as well as
70 the increasing occurrence of CP- versus EP-events¹³⁻¹⁶.

71

72 Studying ENSO diversity has however been largely limited by various technical shortcomings.
73 Such studies are traditionally based on several indices of tropical Pacific SSTa, designed to
74 monitor the variability of either a “canonical” ENSO or two extreme ENSO flavours³³⁻³⁷. Yet,
75 these indices emphasize El Niño events, while La Niña events, which are associated with

76 weaker anomalies than El Niño events³⁸, are typically located further West⁷ and tend to show
77 a more limited range of pattern diversity³⁹, have received less attention. Hence, traditional
78 indices tend to neglect the existing asymmetry between warm- and cold-phases, and between
79 CP- and EP-events. Besides, most of these indices are significantly inter-correlated (Fig.1a),
80 suggesting that they provide redundant information on ENSO. More importantly, the
81 probability distribution of the peak location of SSTa over the tropical Pacific (when each index
82 is exceeding $\pm 0.5^\circ\text{C}$ standard deviation; Fig.1b), indicates that most of these indices are neither
83 representing solely CP- and EP-events, but rather different combinations of both ENSO
84 flavours.

85 **#Figure 1#**

86 It is therefore essential to develop a new framework allowing for a more precise assessment of
87 changes in the location and intensity of warm- and cold ENSO events. In this regard, the
88 “Center of Heat Index” (CHI) provided the basis for a more flexible framework, allowing the
89 longitudinal centre of SSTa to vary as a function of time instead of being geographically
90 fixed^{24,25}. Yet, the CHI approach defines El Niño (La Niña) events based on anomalously warm
91 (cold) areas over very large longitudinal extents ($> \sim 5550\text{km}$), hereby yielding a very smooth
92 representation of ENSO diversity, and limiting the detectable ranges of spatial patterns. Here,
93 we introduce a novel “non-parametric” framework to allow for a more precise assessment of
94 probabilistic changes in ENSO diversity, notably in event locations and intensity (cf. Methods).
95 This new framework is first applied to a suite of observational datasets, including century-long
96 reconstructions, reanalysis and high-resolution satellite-derived estimates (cf. Supplementary
97 Table 1), to identify potential long-term changes in the likelihood of El Niño and La Niña
98 location and intensity, and discuss their associations with decadal climate variability. The same
99 framework is then applied to the two latest multi-model ensembles, *i.e.* CMIP5⁴⁰ and CMIP6⁴¹
100 (cf. Supplementary Table 1), to examine how model fidelity in simulating ENSO diversity is

101 influenced by using an approach that allows for a continuum of patterns, rather than relying on
102 a more rigid bimodal view of the ENSO phenomenon. Historical and multi-centennial pre-
103 industrial control simulations (piControl: 400–1200 years, radiative forcing fixed at the 1850
104 conditions) are used to examine whether robust decadal variations can be found in the absence
105 of anthropogenic influences (piControl) or under historical radiative forcing (historical). The
106 large-scale climate patterns associated with decadal variations in ENSO diversity are examined
107 in both observations and in the climate models that most realistically simulate ENSO diversity
108 and its low-frequency variability in pre-industrial and historical periods. The same models are
109 then used to assess how ENSO diversity is projected to change in the future. In particular, we
110 address two questions: i) do ENSO events really strengthen and shift westward in the 21st
111 century? ii) if so, is that true for both El Niño and La Niña events?

112

113 **Results**

114 **Observed changes in the likelihood of ENSO location and intensity**

115 The average distribution of ENSO location and intensity in 20-year overlapping periods
116 between 1850 and 2017, is examined using five observational datasets (Fig. 2).

117 **#Figure 2#**

118 On average, El Niño events tend to be located over three preferential regions (Fig. 2a): i) in the
119 central Pacific (~166°W; CP-Niño); ii) in a region corresponding to a “canonical” pattern
120 (~118°W; Canonical-Niño); iii) off the coast of southern America, in the eastern Pacific (~
121 85°W; EP-Niño). EP-Niño, or coastal-Niño⁴², are much less likely in all datasets, especially in
122 the satellite-derived data (OISST.v2; Fig. 2a, top-left). Accounting for temporal changes in the
123 probability distribution of all datasets, we identify a coherent and progressive shift to
124 predominant CP-Niño event over the course of the 20th century (Fig. 2a, bottom-left). La Niña
125 also appears characterized by three preferential locations, with no significant differences in the

126 probability distribution from one dataset to another (Fig. 2b, top-left). CP-Niña events seem
127 systematically more likely than Canonical-Niñas, which are in turn more likely than EP-Niñas
128 (Fig. 2b, top-left). Looking at temporal changes in the statistical distribution across all datasets,
129 coherent low-frequency variations emerge in the most likely locations of La Niña (Fig. 2b,
130 bottom-left). CP-Niña events are more frequent in the 1930s-40s and from the 1970s than
131 during the 1950s-60s (Fig. 2b, bottom-left).

132

133 All observational datasets show quasi-normal distributions for event intensity, converging
134 toward SSTa of $+0.86^{\circ}\text{C}$ and -0.9°C for El Niño and La Niña events, respectively (Fig. 2a-b,
135 top-right). In all observational datasets, the probability distribution of La Niña intensity shows
136 relatively small variations over time (Fig. 2b, bottom-right), while decadal variations prevail
137 for El Niño intensity (Fig. 2a, bottom-right). Weaker El Niño are more likely in the late 19th
138 century, the 1920s-50s and 1980s-90s, as compared to the early 20th century, the 1960s-70s
139 and post-2000s (Fig. 2a, bottom-right). Both El Niño and La Niña events show increasing
140 intensities over recent decades, and this is associated with more extreme events, as illustrated
141 by the increasing frequency of extreme warm and cold events (Fig. 2a-b, histograms, bottom-
142 left). This result is consistent with coral oxygen isotopic reconstructions³² and simulated long-
143 term future changes^{30,31}. However, unlike the recent increase in the frequency of extreme La
144 Niña, the intensification of El Niño events does not seem to exceed a natural range of variability
145 (Fig. 2a-b, bottom-right). These results, based on multiple and longer observational records,
146 partly corroborate those of a recent study, highlighting more extreme El Niño and La Niña in
147 the 1980s-90s than in the post-2000 period using OISSTv.2⁴³.

148

149 Hence, observed ENSO diversity is much broader than previously suggested, and exceeds a
150 bimodal view, consistently with results from neural-network based clustering of equatorial

151 Pacific SSTa⁴⁴. This is particularly true for La Niñas, whose diversity was strongly questioned
152 in previous studies³⁹. More importantly, ENSO-event locations do not follow a normal
153 distribution describing a randomly distributed continuum of events²⁴, converging toward a
154 “canonical” location. Instead, ENSO diversity is clearly linked to low-frequency variations,
155 with multiple preferential locations, which may modulate potential trends in ENSO behaviour.

156

157 **Evaluation of ENSO diversity in climate models within our new framework**

158 We compare the simulated probability distributions of ENSO location and intensity from 26
159 CMIP5 and 28 CMIP6 models to our five observational datasets in Fig. 3.

160

#Figure 3#

161 Most models are capable of simulating a broad range of preferred locations for both El Niño
162 and La Niña (Fig. 3a-b, top), and around 39–60% of simulations do not show significant biases
163 in the mean location of El Niño and La Niña in historical and piControl runs (Supplementary
164 Fig. 1). In particular, two CMIP6 models (IPSL-CM6A-LR and UKESM1-0-LL, one of the
165 MOHC group of models) show a range of locations for both warm- and cold-events that is in
166 good agreement with observations (Fig. 3, top). Similar results are found for CNRM-CM5
167 (leftmost columns of the CNRM group of models), but only for El Niño events (Fig. 3, top).
168 Other models show highly asymmetrical probability distributions, with clear tendencies to
169 favour either EP/Canonical- or CP-events (Fig. 3a-b, top), including some extreme cases (e.g.
170 CSIRO-Mk3-6-0) with events always centred further west than the observational range. The
171 excessive westward extensions of the equatorial SSTa^{26–28} could explain the westward shifted
172 mean location of ENSO in CMIP models. Here only 16–30% of model simulations are
173 concerned by this bias (Supplementary Fig. 1). Nevertheless, there are other models that do not
174 simulate erroneous westward extensions of the equatorial SSTa, but hardly depart from a

175 canonical location (Fig. 3a-b, top; Supplementary Fig. 1), thus showing too limited ENSO
176 diversity.

177

178 Simulated intensity distributions of ENSO are mostly consistent with observations, and tend to
179 follow a quasi-normal distribution in most CMIP5 and CMIP6 models, but clear discrepancies
180 emerge in the mean intensity and the probability of extreme events (Fig. 3a-b, bottom). In 53
181 –66% of the simulations, biases in the mean intensity of ENSO events are non-significant for
182 warm- and cold-events, using both historical and piControl simulations (Supplementary Fig.
183 1). Large and significant overestimations and underestimations nevertheless persist in a little
184 less than half of the models (Supplementary Fig. 1).

185

186 In summary, most models simulate some range of pattern diversity for El Niño and La Niña
187 events. In particular, few models present a range of event locations in relatively good
188 agreement with observations, and minimal biases in their intensity. The most common biases
189 concern either the tendency of models to favour one type of events or the events' intensity.
190 Notably, larger biases are found for the models that produce erroneous westward extensions of
191 SSTa (cf. MIROC6, Supplementary Figs. 2-5).

192

193 **Robust decadal variations in ENSO preferred location and intensity**

194 Here, we use spectral analysis to examine whether robust and significant low-frequency
195 variations are found in the most likely location and intensity of ENSO, in both the four long-
196 term observational datasets, as well as CMIP5 and CMIP6 models. We first examine the
197 timescales on which ENSO behaviour varies using maximum power spectrum (See methods,
198 Fig. 4), a method that accounts for non-stationarity of ENSO spectral characteristics, before

199 comparing the observed and simulated magnitude of decadal variations in location and
200 intensity (Fig. 5).

201 **#Figure 4#**

202 Despite some discrepancies, all observational datasets show significant variations on
203 interdecadal timescale (14–32-yr) based on the 10-yr running mean of most likely location of
204 El Niño and La Niña (Fig. 4a-b, top-right). Using both historical and piControl runs, almost all
205 models also show significant variability on interdecadal timescales in their 10-yr most likely
206 location of ENSO (Fig. 4a-b, top-middle and -left). In addition, 71 and 72 (83 and 87) % of
207 historical (piControl) runs significantly simulate statistically equal decadal variance, as
208 compared to observations, in the locations of El Niño and La Niña, respectively (Fig. 5). Few
209 models show significant biases in the magnitude of decadal variations in event locations (Fig.
210 5): i) 9–25% of models underestimate it, and favour either EP/Canonical- (*e.g.*, CCCma
211 models, CNRM-CM6-1) or CP-ENSO (*e.g.*, CESM2); or ii) 2–11% of models overestimate it,
212 and tend to simulate two extremely distinct modes in the central and eastern Pacific (*e.g.*,
213 MIROC6, NorCPM1; Fig. 3a-b, top).

214 **#Figure 5#**

215 According to previous observational studies⁴⁵, as well as fossil coral oxygen isotope records³²,
216 the observed intensity of ENSO presents significant variability on interdecadal timescales at
217 16-yr and, especially, 32-yr periods (Fig. 5a-b, bottom-right). CMIP5 and CMIP6 also simulate
218 significant interdecadal variability at these timescales (Fig. 5, bottom-middle and -left), in
219 agreement with previous studies using climate models^{17,20,21}. Most models (63–85% in
220 historical and piControl runs) display statistically equal decadal variance in the intensity of
221 both El Niño and La Niña (Fig. 5), in agreement with observations. A small fraction of
222 simulations (12–24% in historical and piControl runs) significantly overestimate the decadal
223 variance in ENSO intensity (Fig. 5), as already reported for CCSM4⁴⁶ and CESM2⁴⁷.

224

225 Thus, our results confirm the existence of a significant interdecadal modulation in ENSO
226 intensity in accordance with several studies based on observations, proxy records and climate
227 models^{17,20,21,24,32,45}. While previous studies reported an underestimation of decadal variability
228 by climate models at both global⁴⁸ and Pacific Ocean^{49,50} scales, this statement does not appear
229 to be true for ENSO diversity in most CMIP5 and CMIP6 models, when considering their non-
230 stationary behaviour (cf. Methods). Our results also reveal, for the first time, significant
231 interdecadal modulations in the maximum likelihood of ENSO locations, which are robust and
232 consistent in both observations and climate models. In addition, although few models show
233 recurrent biases, the majority of models appear capable of simulating realistic magnitudes of
234 decadal variance in ENSO diversity.

235

236 **Large-scale patterns linked decadal variability in ENSO location and intensity**

237 To identify large-scale patterns of variability associated with spatio-temporal variations in
238 ENSO, separately for El Niño years and La Niña years, we compute linear regressions of pan-
239 Pacific SSTa, wind-stress and equatorial 20°C isotherm depth (Z20) on the location and
240 intensity of events, using four long-term observational datasets and 32 historical runs from the
241 IPSL-CM6A-LR large ensemble (Fig. 6). We focus on the Pacific region, as regressed SSTa
242 are much lower, and often non-significant, in the other ocean basins (not shown). Similarly, we
243 choose to focus on the IPSL-CM6A-LR model because it provides a realistic range of locations
244 and intensities for both El Niño and La Niña events, with relatively weak model biases (Figs.
245 3-4). Results obtained using other CMIP5 and CMIP6 models are highly similar, especially for
246 patterns associated with ENSO intensity, and approximate the skill of the SODA.si3 reanalysis
247 (Supplementary Figs. 2-3).

248

#Figure 6#

249 In observations, SST regressions on El Niño longitude yield an EP-type event, with largest
250 anomalies extending westward along the Equator from the coast of South America (Fig. 6a,
251 top-left). The associated strong westerly wind anomalies extend to the eastern Pacific, where
252 the thermocline is significantly deeper, whilst slight, but significant, easterly wind anomalies
253 and shallower thermocline are found in the western Pacific (Fig. 6a, top- and bottom-left).
254 These patterns indicate that El Niño events tend to be located further east when trade-winds
255 weaken (strengthen), and the thermocline is significantly deeper (shallower), over the eastern
256 (western) Pacific; meanwhile, the opposite patterns would be associated with El Niño events
257 located further West. This is consistent with previous studies stressing the importance of the
258 initial zonal thermocline slope as a discriminating factor for the selection of EP and CP
259 events⁵¹. Compared to regression patterns associated with El Niño longitude, regressions on La
260 Niña longitude show much stronger (weaker) signals in the western-central (eastern) Pacific
261 (Fig. 6a-b, top-left). However, such differences could originate from differences in the
262 probability distributions of El Niño and La Niña locations (Fig. 2a-b, top-left). Regressions on
263 La Niña longitude result in a pattern that is reminiscent of a CP-Niño pattern³⁷, with cold
264 anomalies in the far eastern Pacific and warm anomalies in the central Pacific (Fig. 6b, top-
265 left). In this case, strong westerly wind anomalies and deeper thermocline are found in the
266 central Pacific, where they may contribute to the zonal advective feedback⁵², while weaker
267 easterly anomalies and deeper thermocline are present in the western Pacific (Fig. 6b, top- and
268 bottom-left). Such patterns indicate that La Niña events tend to be located further east when
269 trade-winds strengthen (weaken), and the thermocline is significantly shallower (deeper), over
270 the eastern (western) Pacific; the opposite patterns would thus favour more western La Niña
271 events. In addition, these tropical signals are statistically significantly related to extra-tropical
272 SSTa (Fig. 6a-b): colder (warmer) North Pacific SSTa are found, when El Niño events are
273 located further east (west), and La Niña events are located further west (east). While these

274 results corroborate previous study on changes in the frequency of CP and EP events during
275 different phases of the PDO^{22,53}, such North Pacific SSTa are also consistent with changes in
276 the intensity and location of the Aleutian Low and North Pacific High in response to EP- and
277 CP-Niño⁵⁴. Similar regression patterns are found in IPSL-CM6A-LR, and other models
278 (Supplementary Figs. 2-3), which can produce realistic changes in zonal wind-stress and
279 thermocline depth, associated with shifts in ENSO locations (Fig. 6c). Patterns associated with
280 changes in El Niño and El Niña locations are however much more symmetrical in models than
281 in observation (Fig. 6c; Supplementary Figs. 2-3). Like other models, IPSL-CM6A-LR shows
282 large internal variability in thermocline depth anomalies, with a clear tendency to
283 underestimate thermocline depth anomalies during El Niño events (Supplementary Fig. 4), and
284 this could explain larger ensemble spread in equatorial Pacific SSTa associated with shifting
285 ENSO locations (Fig. 6c). The North Pacific anomalies associated with ENSO locations are
286 also significant in IPSL-CM6A-LR (Fig. 6c), like in many other models (Supplementary Fig.
287 3). These relationships between ENSO and Pacific extra-tropical variability however show
288 large ensemble spread in IPSL-CM6A-LR (Fig. 6c), highlighting that these relationships are
289 highly sensitive to internal variability, as suggested in previous studies^{22,55}.

290

291 Looking at regressed patterns associated with event intensity, patterns of SST anomalies are
292 more in line with canonical events, extending in the central-eastern Pacific, for both El Niño
293 and La Niña (Fig. 6a-b, top-right). In addition, we found that observed El Niño (La Niña) is
294 more intense when the mean thermocline is deeper (shallower) and the trade-winds are
295 consistently weaker (stronger) over the equatorial Pacific (Fig. 6a-b, top- and bottom-right).
296 Compared to the large-scale patterns associated with ENSO locations, changes in ENSO
297 intensity are associated with larger wind-stress and thermocline depth anomalies over the
298 central-eastern equatorial Pacific (Fig. 6a-b). ENSO intensity also appears associated with

299 extra-tropical SST and wind anomalies that are more symmetric about the Equator compared
300 to those associated with the location (Fig. 6a-b), and are somewhat reminiscent of the extra-
301 tropical signature of the Interdecadal Pacific Oscillation⁵⁶ (IPO). Other studies discussed the
302 separate importance of North and South Pacific climate variability on ENSO intensity at
303 interannual to decadal timescales^{55,57}. Although it systematically underestimates both zonal
304 wind-stress and Z20 anomalies compared to observations (Supplementary Fig. 5), IPSL-
305 CM6A-LR exhibits large-scale anomalies associated with event intensity that are similar to
306 observations (Fig. 6c). Other models also show similar results (Supplementary Figs. 2-3). Most
307 of them simulate coherent changes in wind-stress anomalies and thermocline depth anomalies
308 over the equatorial Pacific, as well as extra-tropical anomalies comparable to observations,
309 during El Niño and La Niña events. Interestingly, IPSL-CM6A-LR shows very little ensemble
310 spread in equatorial Pacific SSTa, while the strength of extra-tropical anomalies and equatorial
311 thermocline responses strongly differ from one simulation to another (Fig 6c).

312

313 **Impact of decadal variations on future scenarios for ENSO diversity**

314 We next examine ENSO location and intensity in climate change projections, using a set of
315 models that produce variability in ENSO diversity closer to observations during the historical
316 period (namely, IPSL-CM6-LR, UKESM-1-0-LL and CNRM-CM5; Fig. 7). A comparison of
317 future scenarios of ENSO diversity in other models, favouring either EP- and CP-ENSO during
318 historical and pre-industrial periods, is given in Supplementary Fig. 6.

319

320 According to IPSL-CM6-LR and UKESM-0-LL, most ensemble members converge to more
321 CP-ENSO over the second half of the 21st century (Fig. 7). This shift to more westward events
322 appears quite early in IPSL-CM6-LR, while it only emerges in the second half of the 21st
323 century in UKESM1-0-LL, as the first half of the 21st century is dominated by decadal

324 variations (Fig. 7). Such decadal variations remain stronger than potential trends throughout
325 the 21st century in CNRM-CM5 (Fig. 7). By contrast, the last generation of the same model
326 (*i.e.* CNRM-CM6-1), which underestimates decadal variability (Fig. 5), shows a clear shift
327 toward more CP-ENSO in the second half of the 21st century (Supplementary Fig. 6). Future
328 pathways for both El Niño and La Niña locations are strongly dependent on the magnitude of
329 decadal variations, and on the ability of state-of-the-art models to reproduce them. Hence,
330 projections of ENSO diversity show significant discrepancies among models, partly due to
331 models' limitations in accurately representing ENSO diversity, and its variability (as illustrated
332 with MIROC6 and CESM2; Supplementary Fig. 6). Nevertheless, our results overall strongly
333 suggest a shift toward more CP-ENSO as a response to increased radiative forcing over the 21st
334 century (Fig. 7; Supplementary Fig. 6). This corroborates previous hypotheses on the recent
335 increase in the frequency of CP-ENSO^{13–16}.

336
337 While previous studies suggested an intensification of both El Niño and La Niña events over
338 the 21st century^{30,31}, such trends are hardly distinguishable in models producing realistic ENSO
339 diversity, according to our framework (Fig. 7). In most models, event-intensity and the
340 frequency of extreme events appear, at least, as variable in the 21st century as during the
341 historical period (Fig. 7). However, some models, such as IPSL-CM6-LR (in the second half
342 of the 21st century; Fig. 7, left) and MIROC6 (from the early- to mid-20th century;
343 Supplementary Fig. 6, middle), do show an intensification of ENSO events. In addition, as
344 highlighted in previous studies^{30,31}, those models show an increase in the frequency of extreme
345 events (Fig. 7; Supplementary Fig 6). Although the reliability of MIROC6 simulations is
346 questionable, considering their generally weaker performances in simulating event-location,
347 their results suggest a potential role of anthropogenic climate change in altering ENSO intensity
348 over the 21st century. Thus, our results highlight that future changes in ENSO characteristics

349 are not necessarily monotonic, as usually assumed, but may undergo large-amplitude decadal
350 variations, leading to the suppression or enhancement of the impact of anthropogenic climate
351 change on ENSO diversity from one decade to another.

352

353

354 **Discussion**

355 To overcome existing limitations in analysing ENSO diversity, this study introduces a new
356 “non-parametric” framework that enables analysis of probabilistic changes in the location and
357 intensity of warm and cold ENSO events. Using multiple century-long observational datasets
358 and state-of-the-art climate models (namely, CMIP5 and CMIP6 ensembles), we first identified
359 robust long-term changes and variability in the likelihood of El Niño and La Niña location and
360 intensity. Although the majority of models favour either EP/Canonical- or CP-ENSO, we found
361 that ENSO diversity is closely linked to significant decadal variations in both observations and
362 climate models. These decadal variations do not only modulate event-intensity, as already
363 highlighted in many studies^{17,20,21,45}, but also affect event-location, converging toward multiple
364 preferential locations in the central and eastern Pacific.

365

366 Despite large underestimations in equatorial zonal wind-stress and thermocline response, we
367 identified robust large-scale patterns associated with long-term changes in ENSO location and
368 intensity using observations and climate models. On the one hand, long-term changes in event-
369 location are associated with zonal perturbation in equatorial wind-stress, which, according to
370 previous studies^{22,53,55}, may be related to the North Pacific climate variability, and with
371 modulations of the thermocline response. On the other hand, long-term changes in event-
372 intensity are associated with strong equatorial wind-stress and thermocline response, whose
373 variability appears associated with the North and South Pacific climate variability.

374

375 The analysis of a realistic set of climate models in terms of ENSO diversity and its variability
376 indicates that magnitude of such decadal variations in the likelihood of ENSO locations and
377 intensity appears even more pronounced than any trend induced by anthropogenic climate
378 change, at least over the first half of the 21st century. Nevertheless, our results strongly suggest
379 a tendency toward more CP-ENSO in response to anthropogenic climate change, which appears
380 more likely over the second half of the 21st century. Similarly, while previous studies suggested
381 an intensification of both El Niño and La Niña events over the 21st century^{30,31}, such trends are
382 only detected in few models using our framework. In most CMIP5 and CMIP6 models, any
383 potential trends in ENSO intensity, which might be attributed to anthropogenic climate change,
384 appear strongly modulated by decadal variations. Our results thus highlight that future
385 scenarios for ENSO diversity, concerning either event-location or event-intensity, strongly
386 depend on the magnitude of decadal variations, as well as the ability of climate models to
387 reproduce them realistically over the 21st century. Although the nature of such decadal
388 variations is not completely understood^{17,19}, and could involve non-linear interactions between
389 natural variability and anthropogenic climate change⁵⁸, our study provides a new perspective
390 for assessing changes in ENSO behaviour on multiple timescales in a changing climate.

391

392 **Methods**

393 **Observational reference datasets**

394 We use five observational datasets, covering all the different ways to reconstruct long-term
395 variability for SST, as well as different resolutions (Supplementary Table 1). This includes
396 three observational reconstructions based on empirical orthogonal functions/teleconnections
397 (EOF/EOTs), spanning the period 1870-2018: i) the extended reconstructed SST version 5⁵⁹
398 (ERSST.v5); ii) the Centennial in-situ Observation-Based Estimates⁶⁰ (COBESST.v2); iii) the

399 Hadley Centre SST data set⁶¹ (HadSST1). As the use of EOF/EOTs might lead to underestimate
400 ENSO diversity in the 19th and early 20th centuries²⁴, observational reconstructions are
401 compared to the eight-member ensemble of ocean reanalysis generated using the Simple Ocean
402 Data Assimilation system with sparse observational input version 3⁶² (SODA.si3) between
403 1870 and 2015. Since the use of satellite observations at the end of 20th century is known to
404 result in a cold bias in HadSST1 and COBESST.v2⁶³, the optimum interpolation SST version
405 2⁶⁴ (OISST.v2) is used for comparison between 1981 and 2018.

406

407 To examine the potential large-scale patterns associated with changes in the ENSO spatio-
408 temporal variability, surface wind-stress was derived from surface zonal and meridional winds
409 for the period 1870-2015, using the NOAA-CIRES-DOE Twentieth Century Reanalysis
410 version 3⁶⁵ (NOAA-20CR.v3). The NOAA-20CR.v3 uses SODA.si3 and HadSST1 as
411 boundary forcing, and therefore provides consistent atmospheric circulations for that SST
412 datasets. Because subsurface potential temperature data are not currently available in
413 SODA.si3, we use SODA.v2.2.4, with NOAA-20CR.v2 as boundary forcing, to provide the
414 most consistent estimate of thermocline depth, using the 20°C isotherm depth (Z20) as a proxy.

415

416 **CMIP5/6 simulations**

417 We use 95 ensemble members of historical simulations from 26 CMIP5 models⁴⁰, and 250
418 members from 28 CMIP6⁴¹ models, together with longer piControl runs (Supplementary Table
419 1), to evaluate how climate models perform in simulating ENSO diversity. Each individual
420 member of historical simulations allows inferring climate variability from the mid-19th to the
421 early-21st century, due to changes in anthropogenic and natural forcings, while accounting for
422 uncertainties associated with internal variability⁶⁶. Similarly, piControl simulations enable
423 assessing the uncertainties associated with the limited length of reliable historical records. In

424 addition, to discuss the implications of our results for future scenarios of ENSO diversity, we
425 use the highest emission scenario or forcing level (8.5W.m^{-2}), *i.e.* the Representative
426 Concentration Pathway RCP8.5 in CMIP5 models, and the Shared Socio-economical Pathway
427 5 that updates the highest forcing level, *i.e.* 8.5W.m^{-2} (SSP5–85) in CMIP6 models. The
428 number of available realisations is substantially lower in future scenarios than historical runs
429 (Supplementary Table 1). Monthly fields of SST, zonal and meridional wind-stress and
430 potential temperature (from which we estimated the thermocline depth from Z20) are used. To
431 ensure consistency with the observational datasets, and to optimise the detection of changing
432 locations and intensity in ENSO, model simulations were all interpolated onto a regular
433 $1.25\times 1.25^\circ$ grid in the ocean and the atmosphere.

434

435 **Examining long-term variability and changes in ENSO location and intensity**

436 To better account for multi-dimensionally varying properties of ENSO, building on the CHI
437 concept^{24,25} and recent recommendations⁶⁷, we introduce a new framework estimating the
438 location and intensity of El Niño and La Niña events at higher-resolution. The location of El
439 Niño (La Niña) events has been defined as the longitudinal location of the maximum
440 (minimum) of SSTa, greater (lower) than 0°C , within a strip that spans the tropical Pacific from
441 150°E to 60°W (excluding the warm-pool region), and averaged between 5°S and 5°N over the
442 boreal winter-months (December to February). Meanwhile, the intensity of events is given by
443 the value of the maximum of SSTa at that location and during the same season. SSTa are
444 calculated by removing the mean and trend of each month. Detrending is performed using a
445 locally estimated scatter-plot smoothing. In addition, to harmonize the results over variable
446 grid-resolutions, and reduce the noise in the signal, the location of the maximum and minimum
447 of SSTa has been estimated using a 2° longitudinal smoothing.

448

449 Using this new framework, we first examine the likelihood of event location and intensity using
450 the probability density functions (PDF). Temporal changes in the likelihood of event location
451 and intensity are first examined by estimating the PDF over every 20-year segments of each
452 observational datasets, and calculating the most likely values (*i.e.* the mode in statistical terms),
453 as well as multi-dataset agreements of high probability (*i.e.* probability exceeding 0.01 and 0.4
454 for event location and intensity, respectively). For each 20-year segment, we also quantify the
455 percentage of disagreement in the probability distribution across observational datasets using
456 a Kolmogorov-Smirnov (KS) test at $p = 0.05$. In addition, we examine whether temporal
457 changes in probability distributions of event intensity are associated with changes in the
458 frequency of extreme El Niño (La Niña) events, by quantifying the 20-year average number of
459 events exceeding (lower than) the 90th (10th) percentile across all datasets.

460

461 Secondly, we further explore the long-term variability using the 10-year most likely location
462 and intensity of El Niño and La Niña events. Continuous wavelet analyses are used to estimate
463 the maximum power spectrum over the full length of observational and simulated records,
464 while accounting for temporal changes⁶⁸. Using continuous wavelet analysis enables to account
465 for non-stationary significant patches of variability, which might not be significant over the
466 full-length of the records, and would not be identified using Fast Fourier Transform.
467 Significance of variability patches are tested at $p=0.05$, based on 1000 Monte-Carlo simulations
468 of the red noise background spectrum.

469

470 **Testing robustness in climate models, identifying large-scale patterns and implications** 471 **for future scenarios**

472 We first examine whether historical and piControl runs, from CMIP5 and CMIP6 models, are
473 able to reproduce a realistic range of locations and intensities for both El Niño and La Niña

474 events, by comparing the simulated PDF to multiple observational datasets. This visual
475 comparison is combined with two statistical tests: i) test for multimodality, i.e. the presence of
476 multiple peaks on the PDF, based on kernel density estimators and the quantification of excess
477 mass⁶⁹; ii) test for difference in the mean using a two-sided student *t*-test (cf. Supplementary
478 Fig. 1). Statistical significance of these tests is calculated using 1000 permutations.

479

480 Secondly, we investigate whether significant decadal variability is detectable in climate
481 models, by comparing the simulated maximum power spectra with observations. We then
482 compare the simulated magnitude of decadal variability to the observed one using the centred

483 ratio of standard deviation ($rSD = 1 - \frac{sd(ENSO_{loc}^{int}[obs]^{10yr})}{sd(ENSO_{loc}^{int}[sim]^{10yr})} \times 100$). Statistical significance is

484 then assessed by performing a two-sided Fisher's F-test at $p=0.05$ between every 100-yr
485 segments through the course of climate simulations and every 100-yr segments in the four
486 longer-term observational SST datasets, from which the rate of success is quantified.

487

488 Thirdly, we compare the observed large-scale patterns associated with long-term variability in
489 the location and intensity of El Niño and La Niña events to historical simulations from a set of
490 climate models. This consists in examining the differences in the patterns of pan-Pacific SST,
491 wind-stress and thermocline depth at the Equator ($5^{\circ}S - 5^{\circ}N$), which are computed using linear
492 regression during composite El Niño and La Niña years, separately. Statistical significance of
493 the regression patterns is calculated using 1000 permutations. We particularly focus on the
494 IPSL-CM6A-LR large ensemble model, which displayed closer similarities to observations in
495 terms of ENSO diversity, but more information about the overall model performances are
496 provided in Supplementary Figs. 2–5 .

497

498 Finally, using RCP8.5 and SSP5–8.5 scenarios from a selected set of climate models, we
499 examine future trajectories for ENSO diversity (*i.e.* location and intensity), and analyse how
500 results differ depending on the skill of those models for simulating ENSO diversity and its
501 variability.

502

503 **Data availability**

504 CMIP5 and CMIP6 data are publicly available at <https://esgf-index1.ceda.ac.uk>. Long-term
505 observational SST datasets, *i.e.* ERSST.v5, COBESST.v2, HadSST1, OISST.v2, are available
506 at <https://climexp.knmi.nl>. SODA.si3 and SODA.v2.2.4 are respectively available from
507 https://psl.noaa.gov/data/gridded/data.20thC_ReanV3.html and
508 <https://iridl.ldeo.columbia.edu/SOURCES/.CARTON-GIESE/.SODA/.v2p2p4>.

509

510 **Code availability**

511 The code used in this study to produce the data analysed were developed in R programming,
512 and can be provided upon reasonable request to BD.

513

514 **References**

- 515 1. McPhaden, M. J., Zebiak, S. E. & Glantz, M. H. ENSO as an Integrating Concept in Earth Science.
516 *Science* **314**, 1740 (2006).
- 517 2. Ng, J. Y., Turner, S. W. D. & Galelli, S. Influence of El Niño Southern Oscillation on global
518 hydropower production. *Environmental Research Letters* **12**, 034010 (2017).
- 519 3. Iizumi, T. *et al.* Impacts of El Niño Southern Oscillation on the global yields of major crops. *Nature*
520 *Communications* **5**, 3712 (2014).
- 521 4. Goddard, L. & Mason, S. Sensitivity of seasonal climate forecasts to persisted SST anomalies. *Climate*
522 *Dynamics* **19**, 619–632 (2002).
- 523 5. Hermanson, L. *et al.* Different types of drifts in two seasonal forecast systems and their dependence on
524 ENSO. *Climate Dynamics* **51**, 1411–1426 (2018).
- 525 6. Dunstone, N. *et al.* Skilful interannual climate prediction from two large initialised model ensembles.
526 *Environmental Research Letters* **15**, 094083 (2020).
- 527 7. Capotondi, A. *et al.* Understanding ENSO Diversity. *Bulletin of the American Meteorological Society*
528 **96**, 921–938 (2015).
- 529 8. Timmermann, A. *et al.* El Niño–Southern Oscillation complexity. *Nature* **559**, 535–545 (2018).
- 530 9. Capotondi, A., Wittenberg, A. T., Kug, J., Takahashi, K. & McPhaden, M. J. ENSO Diversity. in *El*
531 *Niño Southern Oscillation in a Changing Climate* (eds M.J. McPhaden, A. Santoso and W. Cai) (2020).
532 doi:10.1002/9781119548164.ch4.

- 533 10. Cai, W., van Rensch, P., Cowan, T. & Sullivan, A. Asymmetry in ENSO Teleconnection with Regional
534 Rainfall, Its Multidecadal Variability, and Impact. *Journal of Climate* **23**, 4944–4955 (2010).
- 535 11. Preethi, B., Sabin, T. P., Adedoyin, J. A. & Ashok, K. Impacts of the ENSO Modoki and other Tropical
536 Indo-Pacific Climate-Drivers on African Rainfall. *Scientific Reports* **5**, 16653 (2015).
- 537 12. Sohn, S.-J., Tam, C.-Y. & Kug, J.-S. How does ENSO diversity limit the skill of tropical Pacific
538 precipitation forecasts in dynamical seasonal predictions? *Climate Dynamics* **53**, 5815–5831 (2019).
- 539 13. Lee, T. & McPhaden, M. J. Increasing intensity of El Niño in the central-equatorial Pacific. *Geophysical*
540 *Research Letters* **37**, (2010).
- 541 14. Feng, Y., Chen, X. & Tung, K.-K. ENSO diversity and the recent appearance of Central Pacific ENSO.
542 *Climate Dynamics* **54**, 413–433 (2020).
- 543 15. Freund, M. B. *et al.* Higher frequency of Central Pacific El Niño events in recent decades relative to
544 past centuries. *Nature Geoscience* **12**, 450–455 (2019).
- 545 16. Yeh, S.-W. *et al.* El Niño in a changing climate. *Nature* **461**, 511–514 (2009).
- 546 17. Wittenberg, A. T., Rosati, A., Delworth, T. L., Vecchi, G. A. & Zeng, F. ENSO Modulation: Is It
547 Decadally Predictable? *Journal of Climate* **27**, 2667–2681 (2014).
- 548 18. Newman, M., Wittenberg, A. T., Cheng, L., Compo, G. P. & Smith, C. A. The Extreme 2015/16 El
549 Niño, in the Context of Historical Climate Variability and Change. *Bulletin of the American*
550 *Meteorological Society* **99**, S16–S20 (2018).
- 551 19. Capotondi, A. & Sardeshmukh, P. D. Is El Niño really changing? *Geophysical Research Letters* **44**,
552 8548–8556 (2017).
- 553 20. Wittenberg, A. T. Are historical records sufficient to constrain ENSO simulations? *Geophysical*
554 *Research Letters* **36**, (2009).
- 555 21. Choi, J., An, S.-I. & Yeh, S.-W. Decadal amplitude modulation of two types of ENSO and its
556 relationship with the mean state. *Climate Dynamics* **38**, 2631–2644 (2012).
- 557 22. Newman, M. *et al.* The Pacific Decadal Oscillation, Revisited. *Journal of Climate* **29**, 4399–4427
558 (2016).
- 559 23. Hu, S. & Fedorov, A. v. Cross-equatorial winds control El Niño diversity and change. *Nature Climate*
560 *Change* **8**, 798–802 (2018).
- 561 24. Giese, B. S. & Ray, S. El Niño variability in simple ocean data assimilation (SODA), 1871–2008.
562 *Journal of Geophysical Research: Oceans* **116**, (2011).
- 563 25. Ray, S. & Giese, B. S. Historical changes in El Niño and La Niña characteristics in an ocean reanalysis.
564 *Journal of Geophysical Research: Oceans* **117**, (2012).
- 565 26. Capotondi, A., Wittenberg, A. & Masina, S. Spatial and temporal structure of Tropical Pacific
566 interannual variability in 20th century coupled simulations. *Ocean Modelling* **15**, 274–298 (2006).
- 567 27. Bellenger, H., Guilyardi, E., Leloup, J., Lengaigne, M. & Vialard, J. ENSO representation in climate
568 models: from CMIP3 to CMIP5. *Climate Dynamics* **42**, 1999–2018 (2014).
- 569 28. Dieppois, B., Rouault, M. & New, M. The impact of ENSO on Southern African rainfall in CMIP5
570 ocean atmosphere coupled climate models. *Climate Dynamics* **45**, 2425–2442 (2015).
- 571 29. Ham, Y.-G. & Kug, J.-S. How well do current climate models simulate two types of El Niño? *Climate*
572 *Dynamics* **39**, 383–398 (2012).
- 573 30. Cai, W. *et al.* Increased frequency of extreme La Niña events under greenhouse warming. *Nature*
574 *Climate Change* **5**, 132–137 (2015).
- 575 31. Cai, W. *et al.* Increasing frequency of extreme El Niño events due to greenhouse warming. *Nature*
576 *Climate Change* **4**, 111–116 (2014).
- 577 32. Grothe, P. R. *et al.* Enhanced El Niño–Southern Oscillation Variability in Recent Decades. *Geophysical*
578 *Research Letters* **47**, e2019GL083906 (2020).
- 579 33. Rasmusson, E. M. & Carpenter, T. H. Variations in Tropical Sea Surface Temperature and Surface
580 Wind Fields Associated with the Southern Oscillation/El Niño. *Monthly Weather Review* **110**, 354–384
581 (1982).
- 582 34. Kao, H.-Y. & Yu, J.-Y. Contrasting Eastern-Pacific and Central-Pacific Types of ENSO. *Journal of*
583 *Climate* **22**, 615–632 (2009).
- 584 35. Takahashi, K., Montecinos, A., Goubanova, K. & Dewitte, B. ENSO regimes: Reinterpreting the
585 canonical and Modoki El Niño. *Geophysical Research Letters* **38**, (2011).
- 586 36. Trenberth, K. E. & Stepaniak, D. P. Indices of El Niño Evolution. *Journal of Climate* **14**, 1697–1701
587 (2001).
- 588 37. Ashok, K., Behera, S. K., Rao, S. A., Weng, H. & Yamagata, T. El Niño Modoki and its possible
589 teleconnection. *Journal of Geophysical Research: Oceans* **112**, (2007).
- 590 38. Dommenges, D., Bayr, T. & Frauen, C. Analysis of the non-linearity in the pattern and time evolution of
591 El Niño southern oscillation. *Climate Dynamics* **40**, 2825–2847 (2013).
- 592 39. Kug, J.-S. & Ham, Y.-G. Are there two types of La Niña? *Geophysical Research Letters* **38**, (2011).

- 593 40. Taylor, K. E., Stouffer, R. J. & Meehl, G. A. An Overview of CMIP5 and the Experiment Design.
594 *Bulletin of the American Meteorological Society* **93**, 485–498 (2012).
- 595 41. Eyring, V. *et al.* Overview of the Coupled Model Intercomparison Project Phase 6 (CMIP6)
596 experimental design and organization. *Geosci. Model Dev.* **9**, 1937–1958 (2016).
- 597 42. Hu, Z.-Z., Huang, B., Zhu, J., Kumar, A. & McPhaden, M. J. On the variety of coastal El Niño events.
598 *Climate Dynamics* **52**, 7537–7552 (2019).
- 599 43. Rodrigues, R. R., Subramanian, A., Zanna, L. & Berner, J. ENSO Bimodality and Extremes.
600 *Geophysical Research Letters* **46**, 4883–4893 (2019).
- 601 44. Johnson, N. C. How Many ENSO Flavors Can We Distinguish? *Journal of Climate* **26**, 4816–4827
602 (2013).
- 603 45. Sun, F. & Yu, J.-Y. A 10–15-Yr Modulation Cycle of ENSO Intensity. *Journal of Climate* **22**, 1718–
604 1735 (2009).
- 605 46. Deser, C. *et al.* ENSO and Pacific Decadal Variability in the Community Climate System Model
606 Version 4. *Journal of Climate* **25**, 2622–2651 (2012).
- 607 47. Capotondi, A., Deser, C., Phillips, A. S., Okumura, Y. & Larson, S. M. ENSO and Pacific Decadal
608 Variability in the Community Earth System Model Version 2. *Journal of Advances in Modeling Earth*
609 *Systems* **12**, e2019MS002022 (2020).
- 610 48. Mann, M. E., Steinman, B. A. & Miller, S. K. Absence of internal multidecadal and interdecadal
611 oscillations in climate model simulations. *Nature Communications* **11**, 49 (2020).
- 612 49. Ault, T. R., Deser, C., Newman, M. & Emile-Geay, J. Characterizing decadal to centennial variability in
613 the equatorial Pacific during the last millennium. *Geophysical Research Letters* **40**, 3450–3456 (2013).
- 614 50. Power, S., Delage, F., Wang, G., Smith, I. & Kociuba, G. Apparent limitations in the ability of CMIP5
615 climate models to simulate recent multi-decadal change in surface temperature: implications for global
616 temperature projections. *Climate Dynamics* **49**, 53–69 (2017).
- 617 51. Capotondi, A. & Sardeshmukh, P. D. Optimal precursors of different types of ENSO events.
618 *Geophysical Research Letters* **42**, 9952–9960 (2015).
- 619 52. Fang, X.-H. & Mu, M. A Three-Region Conceptual Model for Central Pacific El Niño Including Zonal
620 Advection Feedback. *Journal of Climate* **31**, 4965–4979 (2018).
- 621 53. McPhaden, M. J., Lee, T. & McClurg, D. El Niño and its relationship to changing background
622 conditions in the tropical Pacific Ocean. *Geophysical Research Letters* **38**, (2011).
- 623 54. Taschetto, A. S., Rodrigues, R. R., Meehl, G. A., McGregor, S. & England, M. H. How sensitive are the
624 Pacific–tropical North Atlantic teleconnections to the position and intensity of El Niño-related
625 warming? *Climate Dynamics* **46**, 1841–1860 (2016).
- 626 55. Larson, S. & Kirtman, B. The Pacific Meridional Mode as a trigger for ENSO in a high-resolution
627 coupled model. *Geophysical Research Letters* **40**, 3189–3194 (2013).
- 628 56. di Lorenzo, E. *et al.* ENSO and meridional modes: A null hypothesis for Pacific climate variability.
629 *Geophysical Research Letters* **42**, 9440–9448 (2015).
- 630 57. Liguori, G. & di Lorenzo, E. Separating the North and South Pacific Meridional Modes Contributions to
631 ENSO and Tropical Decadal Variability. *Geophysical Research Letters* **46**, 906–915 (2019).
- 632 58. Cai, W. *et al.* Butterfly effect and a self-modulating El Niño response to global warming. *Nature* **585**,
633 68–73 (2020).
- 634 59. Huang, B. *et al.* Extended Reconstructed Sea Surface Temperature, Version 5 (ERSSTv5): Upgrades,
635 Validations, and Intercomparisons. *Journal of Climate* **30**, 8179–8205 (2017).
- 636 60. Hirahara, S., Ishii, M. & Fukuda, Y. Centennial-Scale Sea Surface Temperature Analysis and Its
637 Uncertainty. *Journal of Climate* **27**, 57–75 (2014).
- 638 61. Rayner, N. A. *et al.* Global analyses of sea surface temperature, sea ice, and night marine air
639 temperature since the late nineteenth century. *Journal of Geophysical Research: Atmospheres* **108**,
640 (2003).
- 641 62. Giese, B. S., Seidel, H. F., Compo, G. P. & Sardeshmukh, P. D. An ensemble of ocean reanalyses for
642 1815–2013 with sparse observational input. *Journal of Geophysical Research: Oceans* **121**, 6891–6910
643 (2016).
- 644 63. Reynolds, R. W., Rayner, N. A., Smith, T. M., Stokes, D. C. & Wang, W. An Improved In Situ and
645 Satellite SST Analysis for Climate. *Journal of Climate* **15**, 1609–625 (2002).
- 646 64. Banzon, V., Smith, T. M., Steele, M., Huang, B. & Zhang, H.-M. Improved Estimation of Proxy Sea
647 Surface Temperature in the Arctic. *Journal of Atmospheric and Oceanic Technology* **37**, 341–349
648 (2020).
- 649 65. Slivinski, L. C. *et al.* Towards a more reliable historical reanalysis: Improvements for version 3 of the
650 Twentieth Century Reanalysis system. *Quarterly Journal of the Royal Meteorological Society* **145**,
651 2876–2908 (2019).

- 652 66. Deser, C., Phillips, A., Bourdette, V. & Teng, H. Uncertainty in climate change projections: the role of
653 internal variability. *Climate Dynamics* **38**, 527–546 (2012).
- 654 67. Planton, Y. Y. *et al.* Evaluating Climate Models with the CLIVAR 2020 ENSO Metrics Package.
655 *Bulletin of the American Meteorological Society* **102**, E193–E217 (2021).
- 656 68. Torrence, C. & Compo, G. P. A Practical Guide to Wavelet Analysis. *Bulletin of the American*
657 *Meteorological Society* **79**, 61–78 (1998).
- 658 69. Ameijeiras-Alonso, J., Crujeiras, R. M. & Rodríguez-Casal, A. Mode testing, critical bandwidth and
659 excess mass. *TEST* **28**, 900–919 (2019).
- 660

661 **Acknowledgements**

662 This work is part of the I-SITE Bourgogne Franche-Comté Junior Fellowship IMVULA
663 (AAP2-JF-06). AC was supported by the NOAA Climate Program Office’s Climate Variability
664 and Predictability (CVP) and Modelling, Analysis, Predictions and Projections (MAPP)
665 programs. The authors would like to thank Noel Keenlyside and Lander Crespo (Geophysical
666 Institute, University of Bergen) for their helpful discussions.

667

668

669

670

671

672

673

674

675

676

677

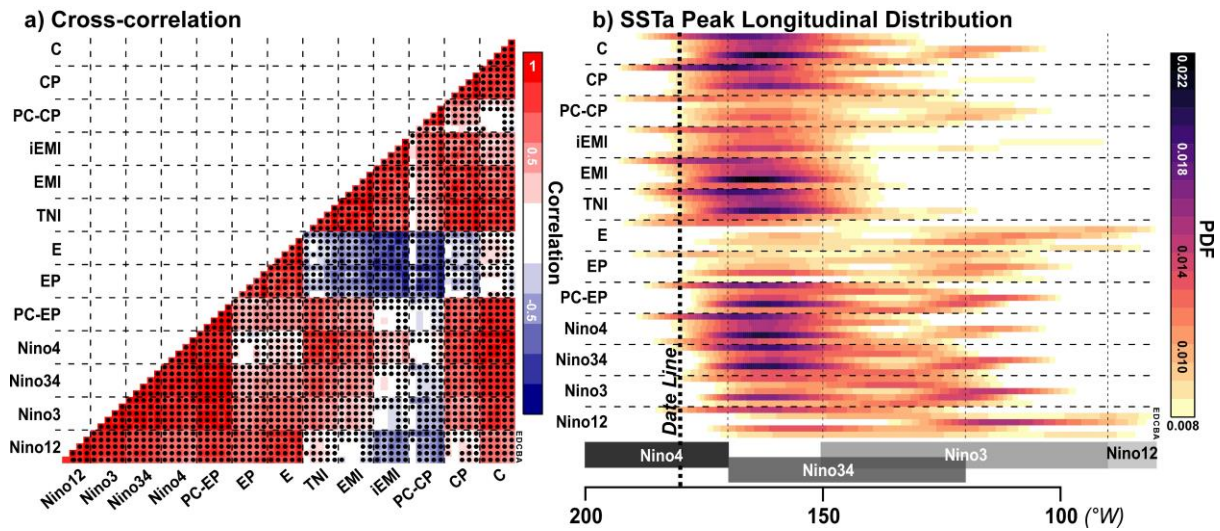
678

679

680

681

682 **Captions**



683

684 **Fig 1. | Relationships between ENSO indices, and their ability to disentangle CP and EP.**

685 (a) Pearson's correlations between 13 ENSO indices (Niño boxes³³; PC-based EP- and CP-
 686 ENSO; TNI³⁶; EMI and iEMI³⁷; EP and CP³⁴; E and C³⁵. Black dots indicate significant
 687 correlations at $p=0.05$, using 1000 phase-randomizations to account for serial correlations. (b)
 688 Probability Density Function (PDF) of the locations of SSTA peaks over the equatorial Pacific
 689 ($5^{\circ}S-5^{\circ}N$; $-210-60^{\circ}W$), when each ENSO index exceeds $\pm 0.5^{\circ}C$ standard deviation. For each
 690 index, each row/column corresponds to a different observational, reanalysis or satellite-derived
 691 dataset (A-E: ERSST.v5, COBESST.v2, HadSST1, SODA.si3, OISST.v2). Correlations are
 692 calculated over their respective common periods (1870-2017 when using observations only,
 693 1870-2015 when using SODA.si3, or 1981-2017 when using OISST.v2). Locations of Niño
 694 boxes, as well as of the date line, are indicative.

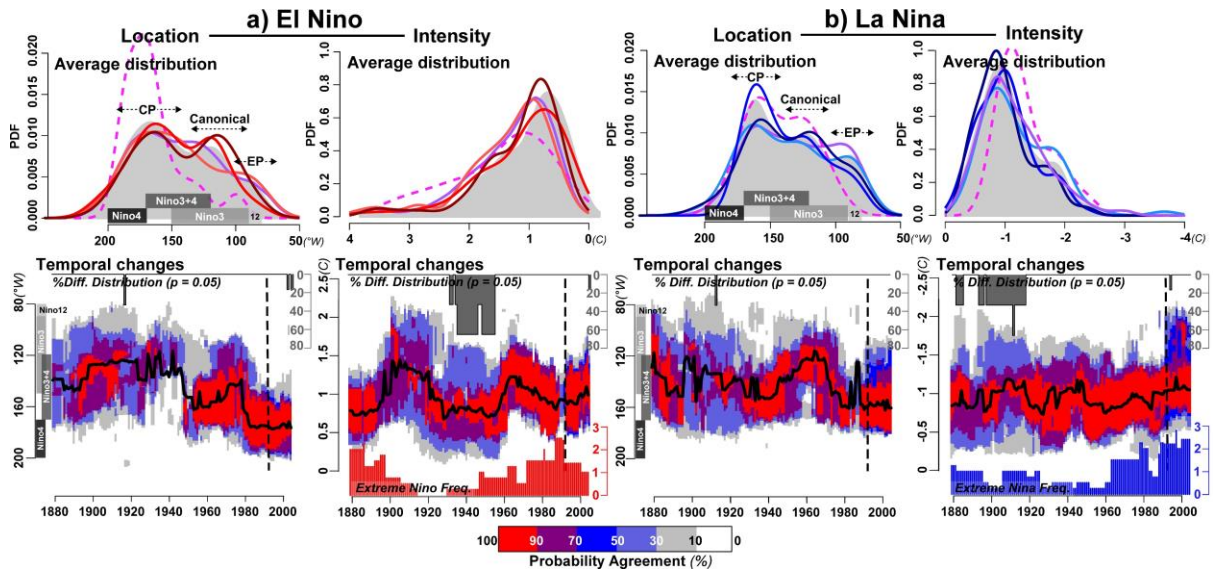
695

696

697

698

699



700

701

Fig 2. | Observed likelihood of ENSO's location and intensity: average distribution and

702

temporal changes. (a) top panels, average probability density function (PDF) of El Niño

703

location (left) and intensity (right). Bottom panels, 20-year running the most likely location

704

and intensity of El Niño (black bold lines), the percentage of agreement of high-probability

705

(*i.e.* PDF exceeding 0.01 and 0.45; colour shades), and average number of extreme Niño events

706

(*i.e.* intensity exceeding the 90th percentile; red histogram) across all observational datasets.

707

(b) same as **(a)** but for La Niña, and extreme La Niña events (*i.e.* intensity lower than the 10th

708

percentile; blue histogram). On top panels, dark grey shading from the top axis indicates the

709

average PDF over all five reference SST datasets, and each individual dataset is displayed in

710

coloured lines (El Niño/La Niña: ERSST.v5 [1850-2017; coral/light blue], COBESST.v2

711

[1850-2017; dark red/dark blue], HadSST1 [1850-2017; red/blue], SODA.si3 [1850-2015;

712

purple solid lines], OISST.v2 [1981-2017; magenta dashed lines]). On bottom panels, grey

713

shading indicates the percentage of observational datasets showing significantly equal

714

distribution at $p=0.05$ according to a Kolmogorov-Smirnov test. Locations of Niño boxes, as

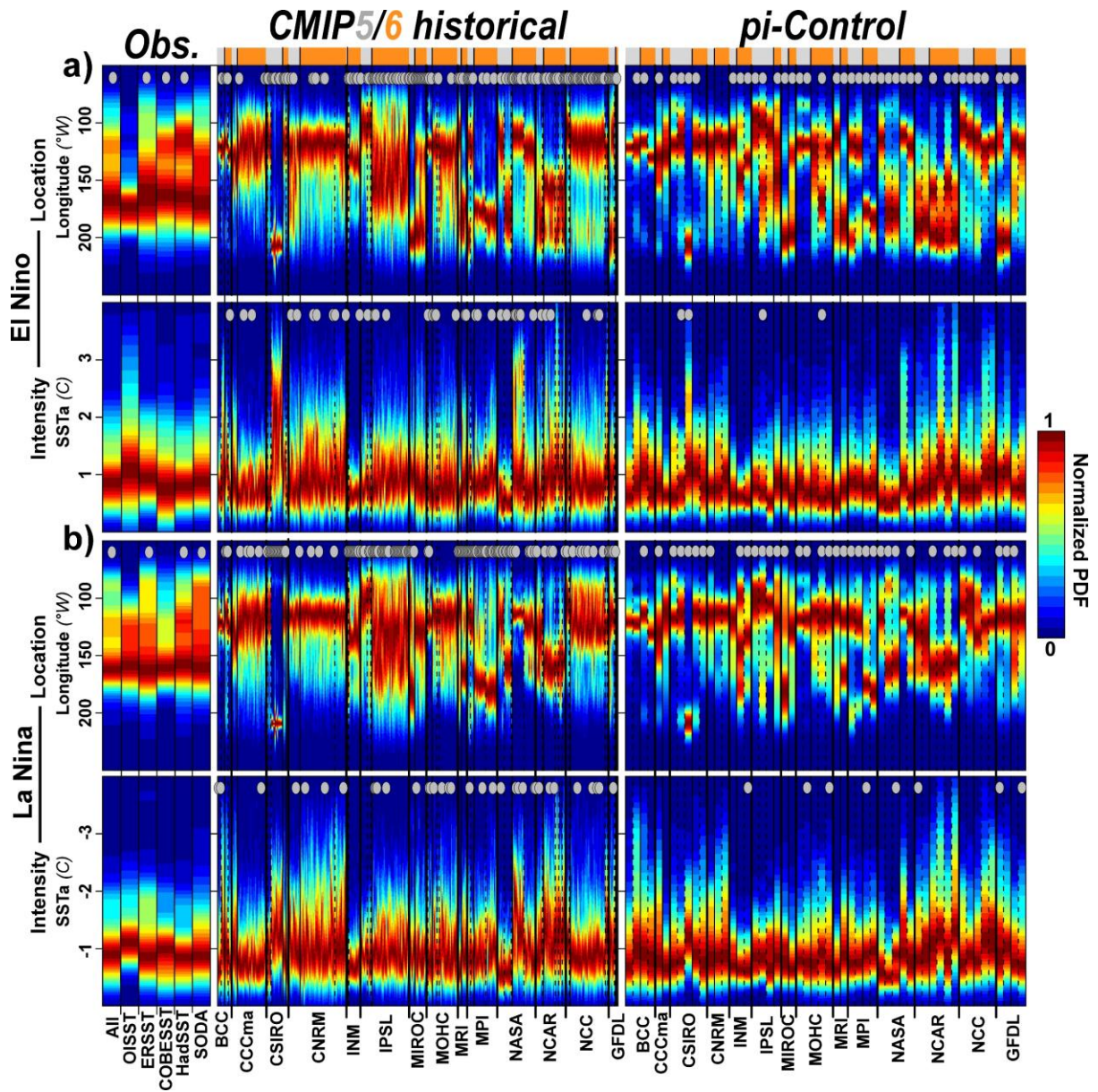
715

well as of the date line, are indicative. Dashed lines delineate the period for which OISST.v2

716

is used (1991-2007, which covers 20-yr periods between 1981-2001 and 1997-21017).

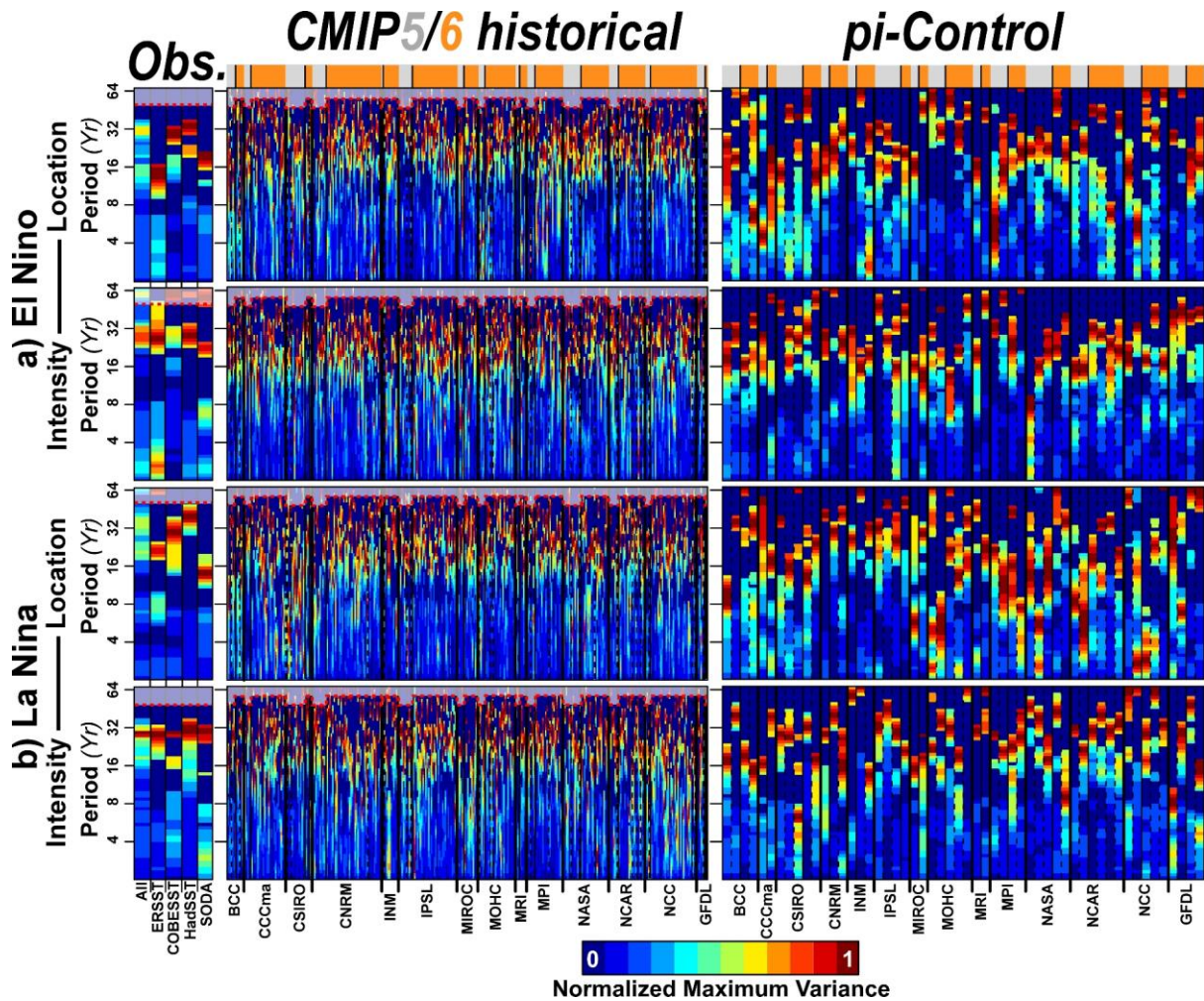
717



718

719 **Fig 3. | Likelihood of ENSO's location and intensity in CMIP5 and CMIP6 models.** (a) top
 720 panels, normalized PDF of El Niño location (top) and intensity (bottom) in all reference
 721 datasets (left), as compared to 95/250 CMIP5/6 historical runs (middle), as well as in 26/28
 722 CMIP5/6 piControl runs (right). (b) same as (a) but for La Niña. On top of each panel and
 723 column, grey dots indicate significant multimodality at $p=0.05$ according to the ACR test⁶⁹,
 724 based on 1000 bootstrap resamples. The normalized PDF is estimated using the full length of
 725 each time series, ranging from 37 years in OISST.v2 to 1200 years in some piControl
 726 simulations. Bold (thin) solid lines separate simulations from different institutions
 727 (generations, i.e.: CMIP5 [grey] and CMIP6 [orange]), while dashed lines separate simulations
 728 from different models.

729



730

731 **Fig 4. | Variability in ENSO's, observed and simulated, most likely location and intensity.**

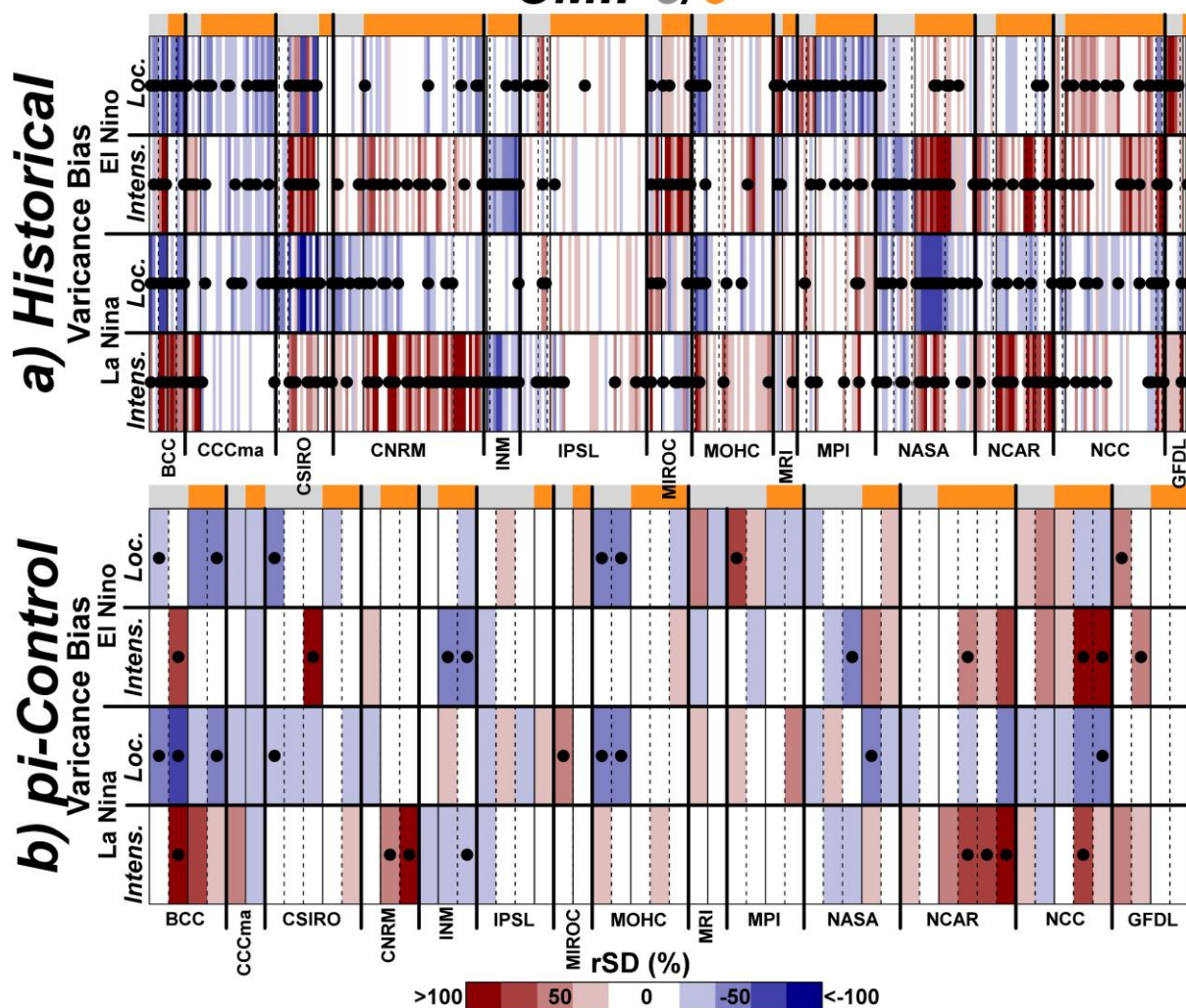
732 **(a)** Maximum power spectrums of the running 10-year El Niño most likely location and
 733 intensity (i.e. the mode), as determined using continuous wavelet analysis, and using four long-
 734 term observational reference datasets (left: ERSST.v5, COBESST.v2, HadSST1, SODA.si3),
 735 95/250 CMIP5/6 historical runs (middle), as well as 26/28 CMIP5/6 piControl runs (right). **(b)**
 736 same as **(a)** but for La Niña. Significance of variability patches are tested at $p=0.05$ based on
 737 1000 Monte-Carlo simulations of the red noise background spectrum. Dashed red lines and
 738 grey shading indicate the area where variability can be underestimated because of edge effects,
 739 wraparound effects and zero-padding. As the continuous wavelet analysis allows to account
 740 for temporal changes the maximum power spectrums are estimated using the full length of each
 741 time series. The maximum power spectrums are weighted by the significance, and only
 742 significant variability is shown.

743

744

745

CMIP5/6



746

747 **Fig 5. | CMIP5/6 bias in decadal variability of ENSO's most likely location and intensity.**

748 **(a)** Average ratio of standard deviation (rSD) between historical runs and observed decadal

749 variance (>10 year) in the running 10-year most likely location and intensity of El Niño and La

750 Niña events. **(b)** same as **(a)** but using pi-Control runs. Statistical significance is assessed by

751 performing a two-sided Fisher's F-test at $p=0.05$ between every 100-yr segments through the

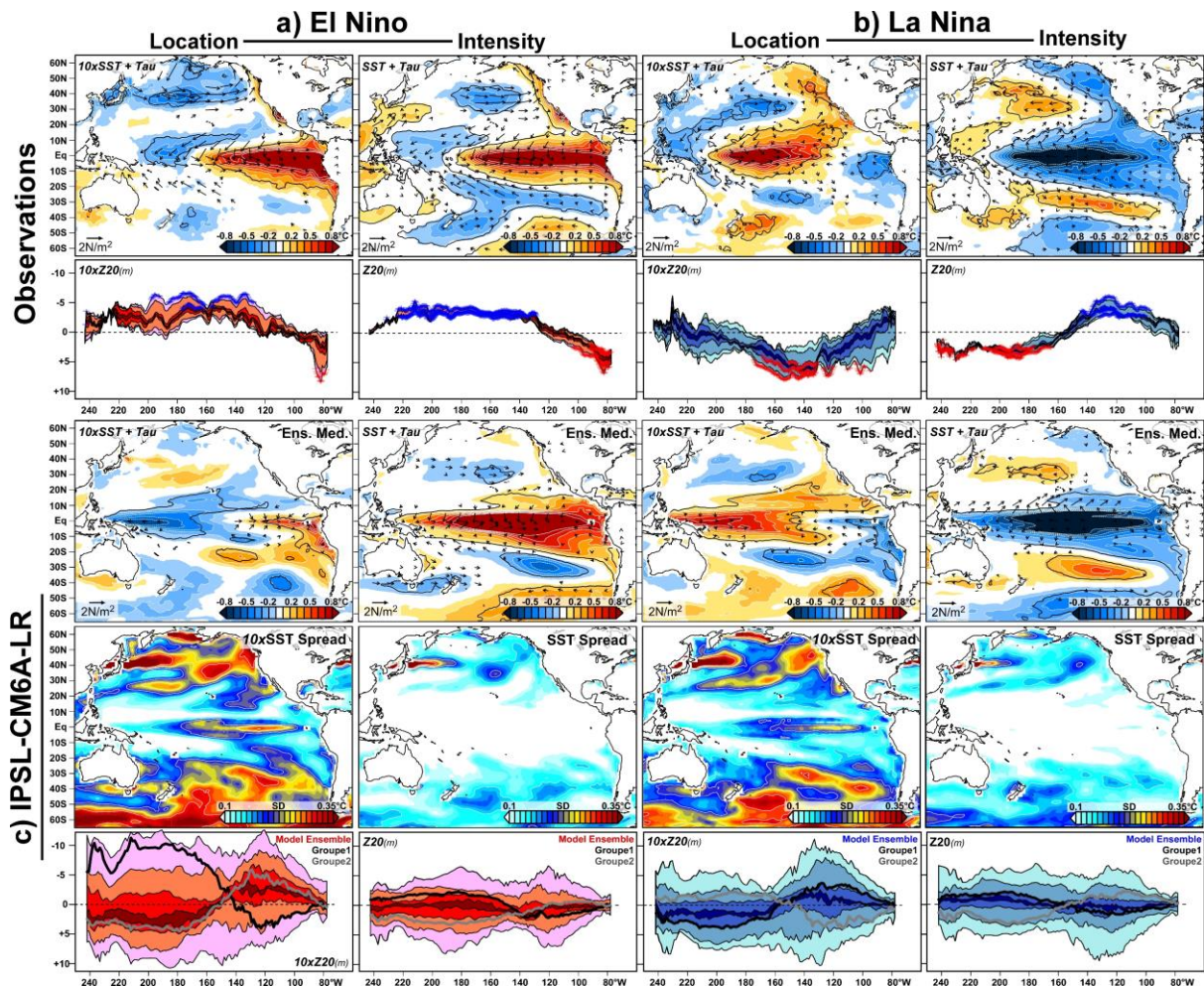
752 course of climate simulations and every 100-yr segments in the four longer-term observational

753 SST datasets (*i.e.* $27,740 \leq n \leq 209,000$ replicates), to quantify a rate of success (*i.e.* the number

754 of times observations and simulations showed equal variance). Black dots highlight simulations

755 for which the rate of success is lower than 10%, showing significantly different variance at

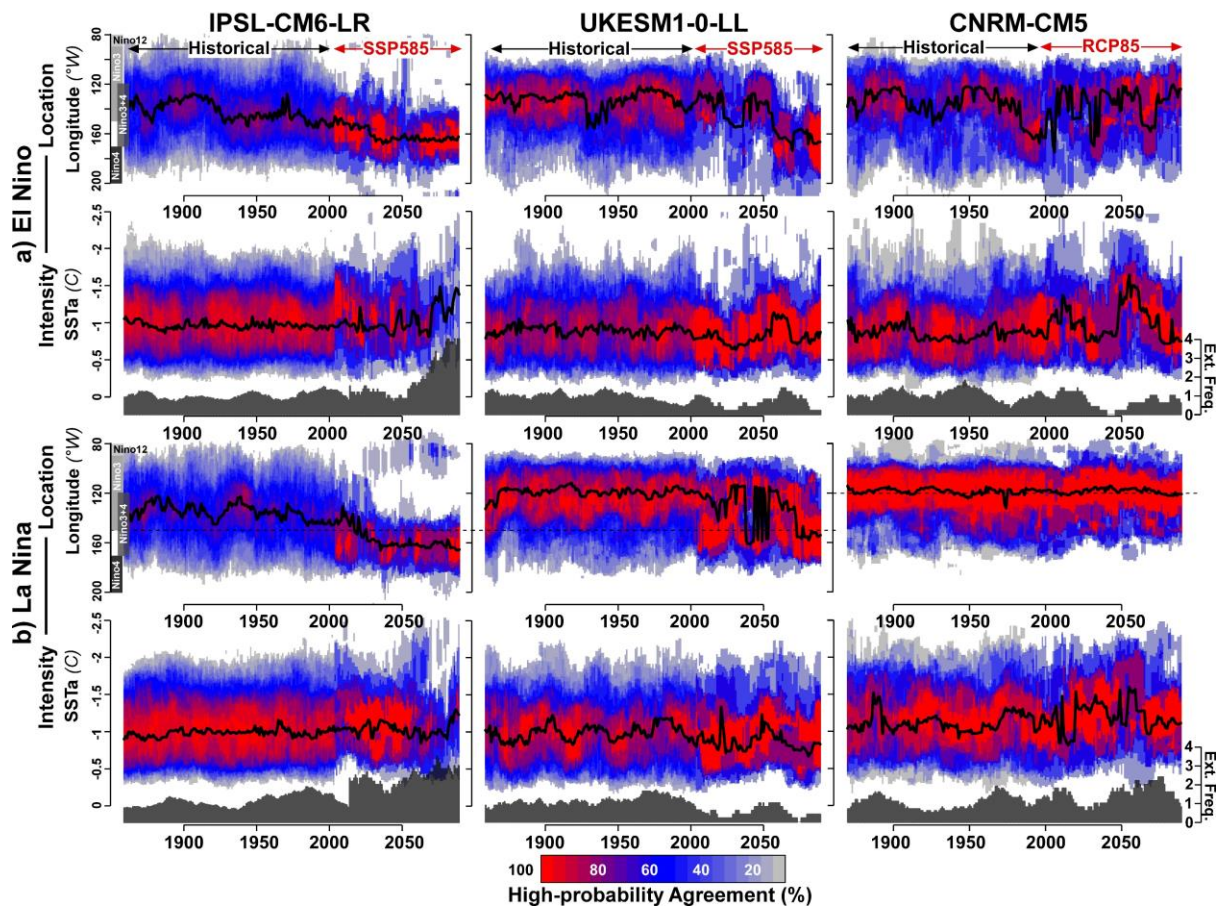
756 $p=0.1$.



757

758 **Fig 6. | Large-scale patterns driving long-term variability in ENSO location and intensity.**

759 (a) Observed regressed SST (blue to red shades), wind-stress (vectors) and Z20 anomalies
 760 (lines) associated with changes in El Niño location (right) and intensity (left) and using multiple
 761 observational data sets (SST: ERSST.v5, COBESST.v2, HadSST1 and SODA.si3; wind-stress:
 762 NOAA-20CR.v3; Z20: SODA.v2.2.4). (b) Same as (a) but for La Niña events. (c) same as (a-
 763 b) but using the IPSL-CM6A-LR large ensemble (32 members). While SST and wind-stress
 764 anomalies are displayed at the pan-Pacific scale based on the median changes in observations,
 765 simulated regressed anomalies are assessed through the ensemble median (top) and ensemble
 766 spread (standard deviation [SD]; middle)]. Z20 anomalies are estimated through the median
 767 changes between 5°S and 5°N (bottom). Red and Blue shades on the Z20 anomalies indicate
 768 the spread between the four SST observational data sets and within the IPSL-CM6A-LR large
 769 ensemble (light to dark: maximum/minimum, 10/90th, 30/70th and 45/55th percentiles), for El
 770 Niño and La Niña, respectively. Group 1 (black lines) and Group 2 (grey lines) illustrate how
 771 two opposed types of equatorial Z20 anomalies influence the ensemble spread. Statistical
 772 significance is assessed at p=0.05 using 1000 permutations, and displayed as black contour for
 773 SSTa, and blue/red crosses for Z20 anomalies. Only significant wind-stress anomalies at
 774 p=0.05 are displayed.



775

776 **Fig 7. | Future scenarios for ENSO diversity in the most realistic models. (a)** 20-year most
 777 likely location (top) and intensity (bottom) of El Niño events (black bold lines), as well as the
 778 percentage of agreement of high-probability (PDF exceeding 0.01 and 0.45; colour shades) in
 779 the IPSL-CM6-LR (left), UKESM1-0-LL (middle) and CNRM-CM5 (right) ensembles. **(b)**
 780 same as **(a)** but for La Niña events. Grey histograms on the bottom axis of the intensity panels
 781 indicate the average number of extreme events (as defined in Fig. 2) within the model
 782 ensemble. SSTa are estimated by removing the 1850–2014 monthly climatology and trend, to
 783 allow comparison with observations. The same baseline period was used to estimate the 90th
 784 and 10th percentiles.

Figures

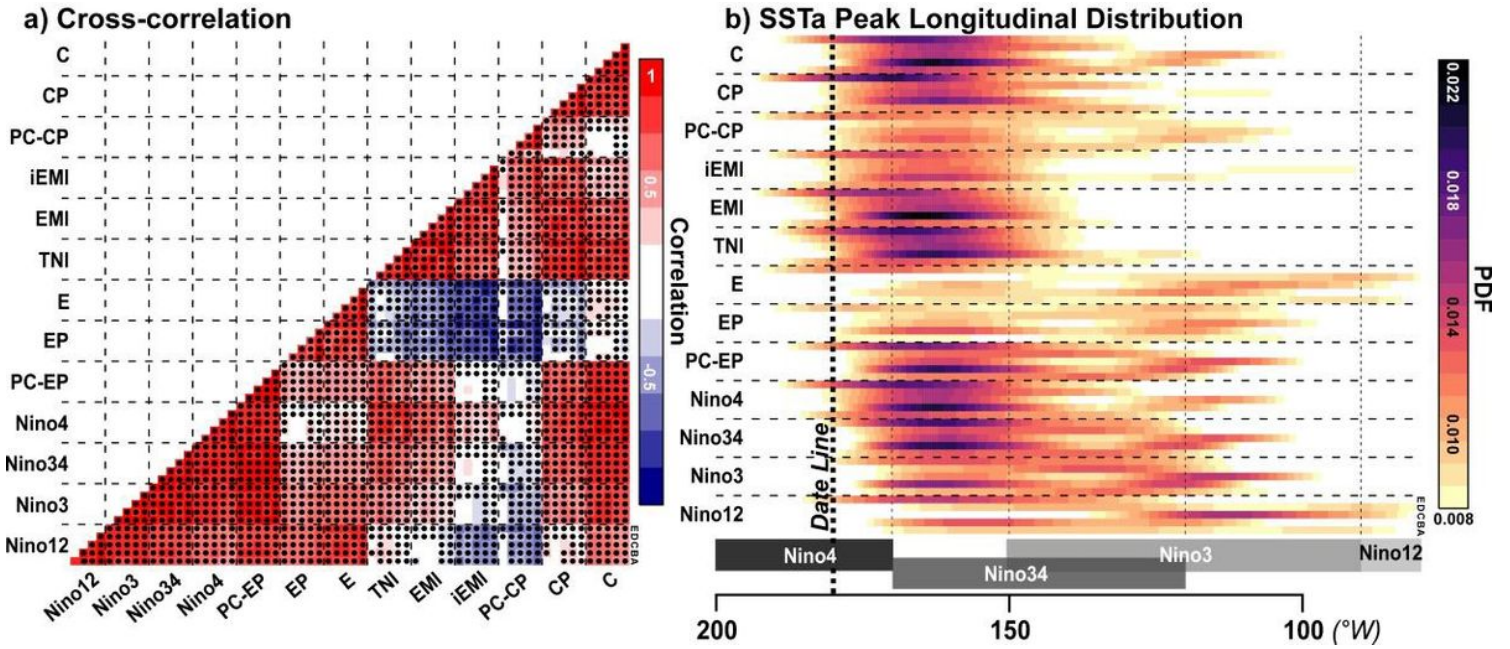


Figure 1

Relationships between ENSO indices, and their ability to disentangle CP and EP. (a) Pearson's correlations between 13 ENSO indices (Niño boxes³³; PC-based EP- and CP-ENSO; TNI³⁶; EMI and iEMI³⁷; EP and CP³⁴; E and C³⁵). Black dots indicate significant correlations at $p=0.05$, using 1000 phase-randomizations to account for serial correlations. (b) Probability Density Function (PDF) of the locations of SSTa peaks over the equatorial Pacific ($5^{\circ}\text{S}-5^{\circ}\text{N}$; $-210--60^{\circ}\text{W}$), when each ENSO index exceeds $\pm 0.5^{\circ}\text{C}$ standard deviation. For each index, each row/column corresponds to a different observational, reanalysis or satellite-derived dataset (A-E: ERSST.v5, COBESST.v2, HadSST1, SODA.si3, OISST.v2). Correlations are calculated over their respective common periods (1870-2017 when using observations only, 1870-2015 when using SODA.si3, or 1981-2017 when using OISST.v2). Locations of Niño boxes, as well as of the date line, are indicative.

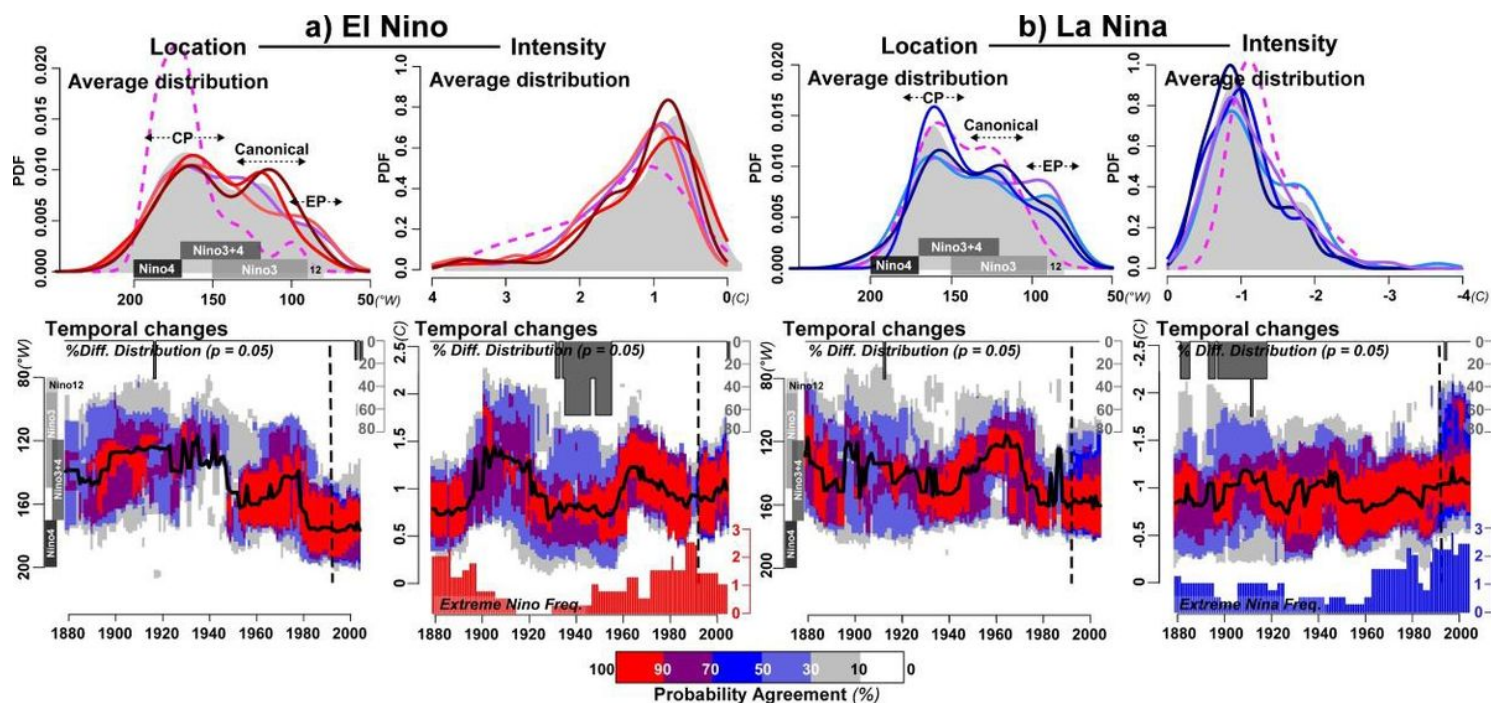


Figure 2

Observed likelihood of ENSO's location and intensity: average distribution and temporal changes. (a) top panels, average probability density function (PDF) of El Niño location (left) and intensity (right). Bottom panels, 20-year running the most likely location and intensity of El Niño (black bold lines), the percentage of agreement of high-probability (i.e. PDF exceeding 0.01 and 0.45; colour shades), and average number of extreme Niño events (i.e. intensity exceeding the 90th percentile; red histogram) across all observational datasets. (b) same as (a) but for La Niña, and extreme La Niña events (i.e. intensity lower than the 10th percentile; blue histogram). On top panels, dark grey shading from the top axis indicates the average PDF over all five reference SST datasets, and each individual dataset is displayed in coloured lines (El Niño/La Niña: ERSST.v5 [1850-2017; coral/light blue], COBESST.v2 [1850-2017; dark red/dark blue], HadSST1 [1850-2017; red/blue], SODA.si3 [1850-2015;purple solid lines], OISST.v2 [1981-2017; magenta dashed lines]). On bottom panels, grey shading indicates the percentage of observational datasets showing significantly equal distribution at $p=0.05$ according to a Kolmogorov-Smirnov test. Locations of Niño boxes, as well as of the date line, are indicative. Dashed lines delineate the period for which OISST.v2 is used (1991-2007, which covers 20-yr periods between 1981-2001 and 1997-21017).

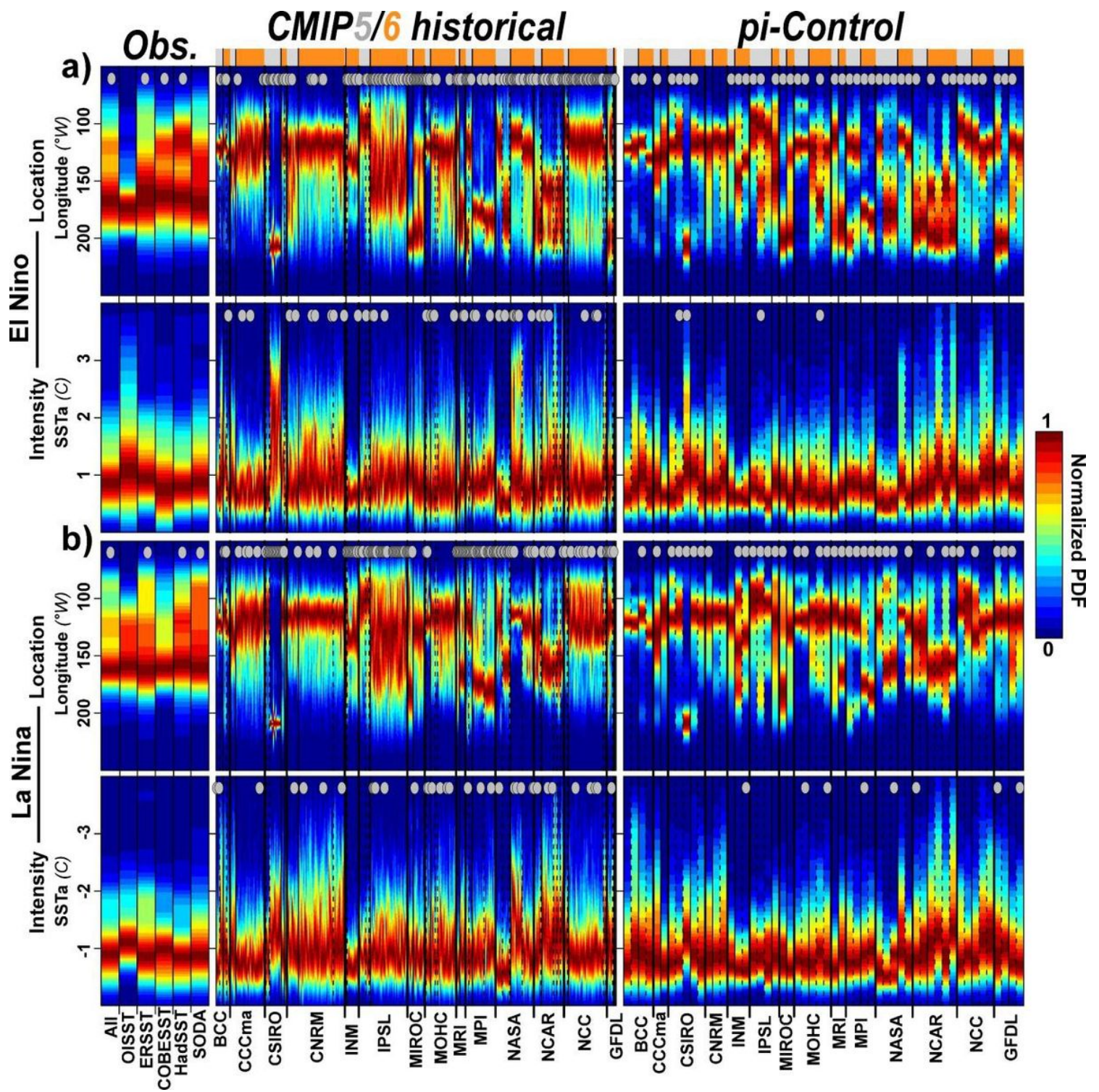


Figure 3

Likelihood of ENSO's location and intensity in CMIP5 and CMIP6 models. (a) top panels, normalized PDF of El Niño location (top) and intensity (bottom) in all reference datasets (left), as compared to 95/250 CMIP5/6 historical runs (middle), as well as in 26/28 CMIP5/6 piControl runs (right). (b) same as (a) but for La Niña. On top of each panel and column, grey dots indicate significant multimodality at $p=0.05$ according to the ACR test⁶⁹, based on 1000 bootstrap resamples. The normalized PDF is estimated using the full length of each time series, ranging from 37 years in OISST.v2 to 1200 years in some piControl

simulations. Bold (thin) solid lines separate simulations from different institutions (generations, i.e.: CMIP5 [grey] and CMIP6 [orange]), while dashed lines separate simulations from different models.

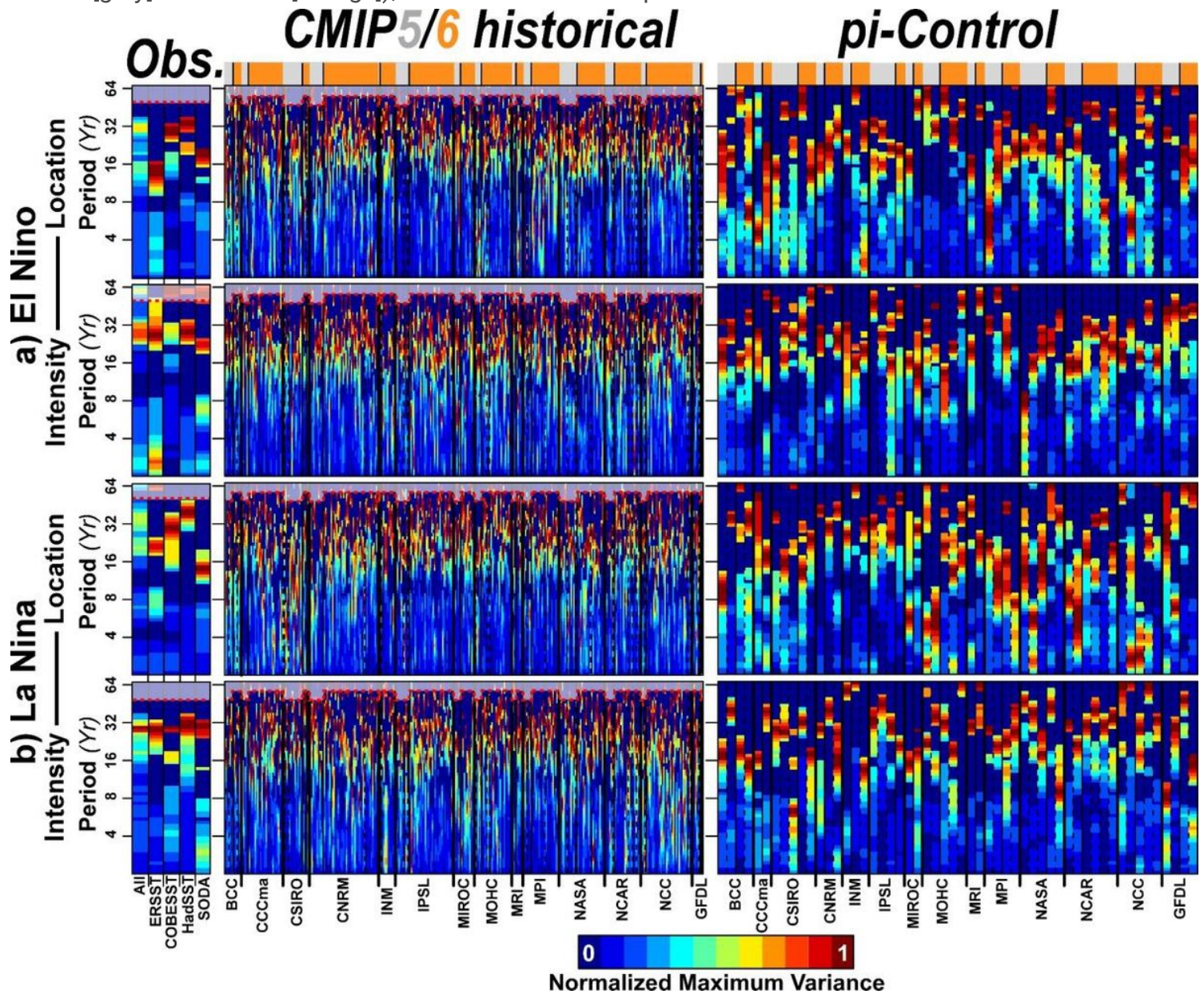


Figure 4

Variability in ENSO's, observed and simulated, most likely location and intensity. (a) Maximum power spectrums of the running 10-year El Niño most likely location and intensity (i.e. the mode), as determined using continuous wavelet analysis, and using four long-term observational reference datasets (left: ERSST.v5, COBESST.v2, HadSST1, SODA.si3), 95/250 CMIP5/6 historical runs (middle), as well as 26/28 CMIP5/6 piControl runs (right). (b) same as (a) but for La Niña. Significance of variability patches are tested at $p=0.05$ based on 1000 Monte-Carlo simulations of the red noise background spectrum. Dashed red lines and grey shading indicate the area where variability can be underestimated because of edge effects, wraparound effects and zero-padding. As the continuous wavelet analysis allows to account for temporal changes the maximum power spectrums are estimated using the full length of each time series.

The maximum power spectrums are weighted by the significance, and only significant variability is shown.

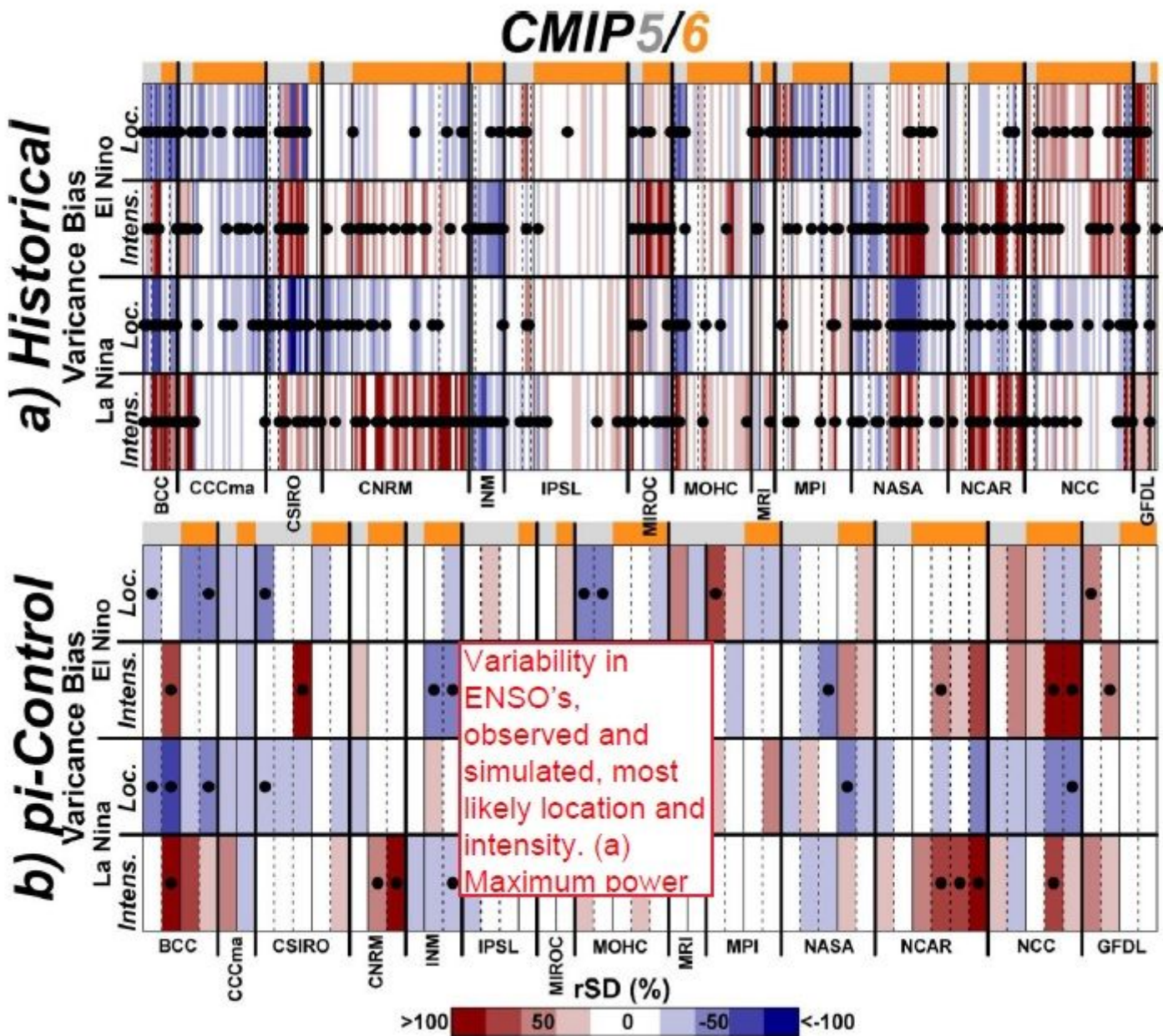


Figure 5

CMIP5/6 bias in decadal variability of ENSO's most likely location and intensity. (a) Average ratio of standard deviation (rSD) between historical runs and observed decadal variance (>10 year) in the running 10-year most likely location and intensity of El Niño and La Niña events. (b) same as (a) but using pi-control runs. Statistical significance is assessed by performing a two-sided Fisher's F-test at $p=0.05$ between every 100-yr segments through the course of climate simulations and every 100-yr segments in the four longer-term observational SST datasets (i.e. $27,740 \leq n \leq 209,000$ replicates), to quantify a rate of success (i.e. the number of times observations and simulations showed equal variance). Black dots

highlight simulations for which the rate of success is lower than 10%, showing significantly different variance at $p=0.1$.

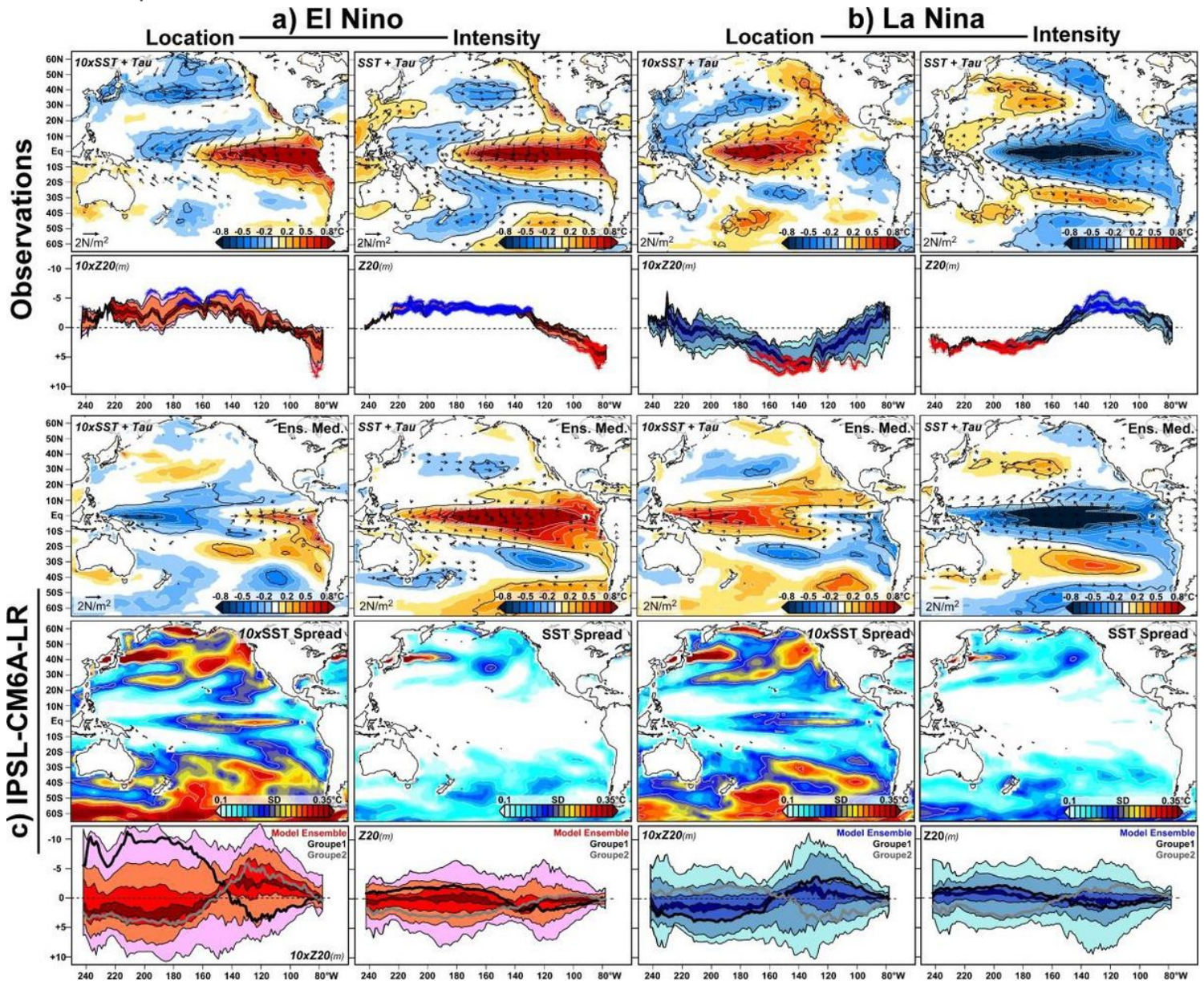


Figure 6

Large-scale patterns driving long-term variability in ENSO location and intensity. (a) Observed regressed SST (blue to red shades), wind-stress (vectors) and Z20 anomalies (lines) associated with changes in El Niño location (right) and intensity (left) and using multiple observational data sets (SST: ERSST.v5, COBESST.v2, HadSST1 and SODA.si3; wind-stress: NOAA-20CR.v3; Z20: SODA.v2.2.4). (b) Same as (a) but for La Niña events. (c) same as (a-b) but using the IPSL-CM6A-LR large ensemble (32 members). While SST and wind-stress anomalies are displayed at the pan-Pacific scale based on the median changes in observations, simulated regressed anomalies are assessed through the ensemble median (top) and ensemble spread (standard deviation [SD]; middle). Z20 anomalies are estimated through the median changes between 5°S and 5°N (bottom). Red and Blue shades on the Z20 anomalies indicate the spread between the four SST observational data sets and within the IPSL-CM6A-LR large ensemble (light

to dark: maximum/minimum, 10/90th, 30/70th and 45/55th percentiles), for El Niño and La Niña, respectively. Group 1 (black lines) and Group 2 (grey lines) illustrate how two opposed types of equatorial Z20 anomalies influence the ensemble spread. Statistical significance is assessed at $p=0.05$ using 1000 permutations, and displayed as black contour for SSTa, and blue/red crosses for Z20 anomalies. Only significant wind-stress anomalies at $p=0.05$ are displayed.

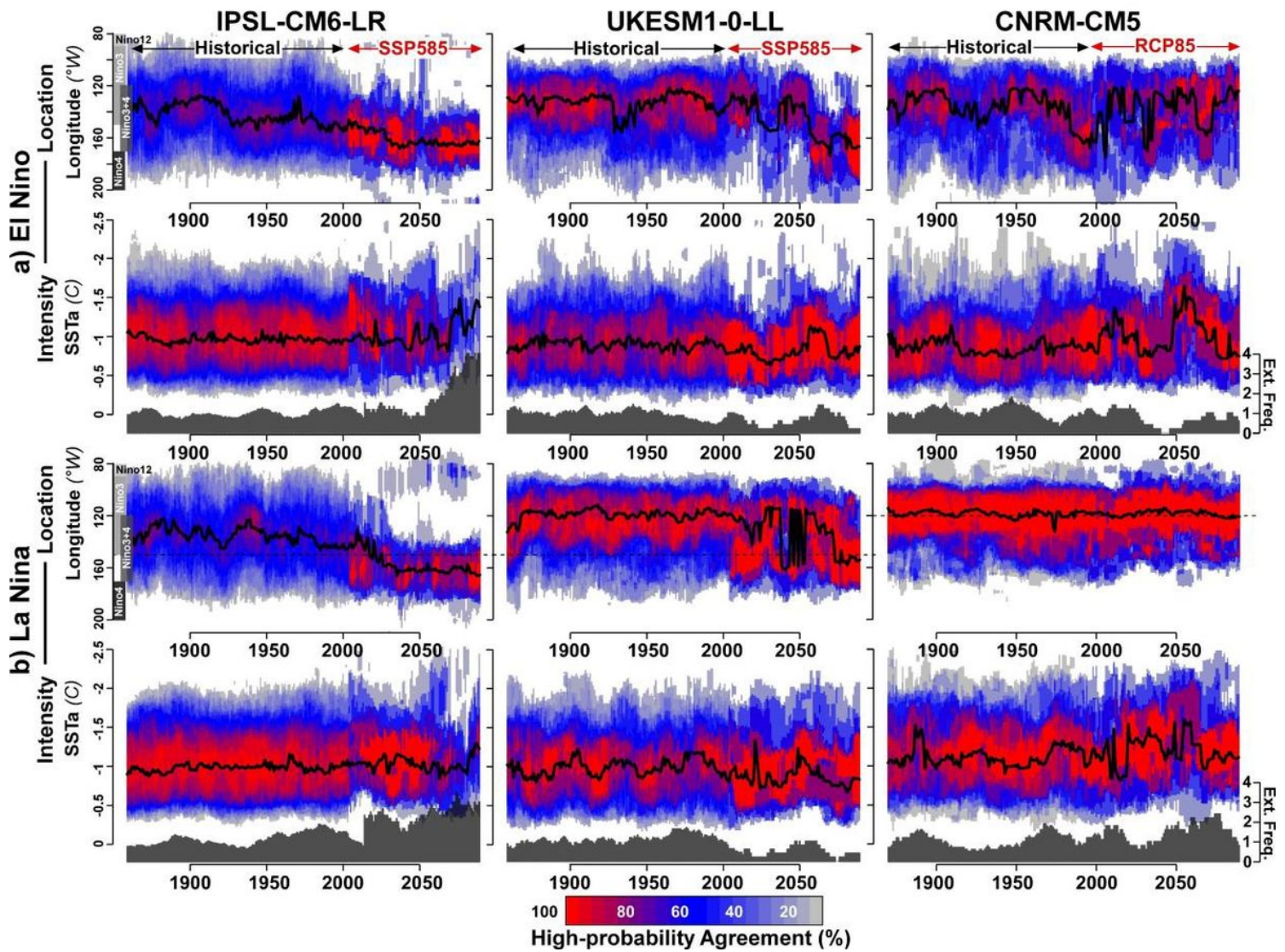


Figure 7

Future scenarios for ENSO diversity in the most realistic models. (a) 20-year most likely location (top) and intensity (bottom) of El Niño events (black bold lines), as well as the percentage of agreement of high-probability (PDF exceeding 0.01 and 0.45; colour shades) in the IPSL-CM6-LR (left), UKESM1-0-LL (middle) and CNRM-CM5 (right) ensembles. (b) same as (a) but for La Niña events. Grey histograms on the bottom axis of the intensity panels indicate the average number of extreme events (as defined in Fig. 2) within the model ensemble. SSTa are estimated by removing the 1850–2014 monthly climatology and trend, to allow comparison with observations. The same baseline period was used to estimate the 90th and 10th percentiles.

Supplementary Files

This is a list of supplementary files associated with this preprint. Click to download.

- [NatCommSupMatDieppoisetal.ENSOContinuum.pdf](#)